Society for
Mathematical
Biology

ORIGINAL ARTICLE

Quantitative Pharmacology Methods for Bispecific T Cell Engagers

Mahdiar Sadeghi[1,2] · Irina Kareva[2,3] · Gleb Pogudin[4] ·
Eduardo D. Sontag[1,3,5]

© The Author(s), under exclusive licence to the Society for Mathematical Biology 2025

Abstract

T Cell Engager (TCE)s are an exciting therapeutic modality in immuno-oncology that acts to bypass antigen presentation and forms a direct link between cancer and immune cells in the Tumor Microenvironment (TME). TCEs are efficacious only when the drug is bound to both immune and cancer cell targets. Therefore, approaches that maximize the formation of the drug-target trimer in the TME are expected to increase the drug's efficacy. In this study, we quantitatively investigate how the concentration of ternary complex and its biodistribution depend on both the targets' specific properties and the design characteristics of the TCE, and specifically on the binding kinetics of the drug to its targets. A simplified mathematical model of drug-target interactions is considered here, with insights from the "three-body" problem applied to the model. Parameter identifiability analysis performed on the model demonstrates that steady state data, which is often available at the early pre-clinical stages, is sufficient to estimate the binding affinity of the TCE molecule to both targets. We used the model to analyze several existing antibodies, both clinically approved and under development, to explore their common kinetic features. The manuscript concludes with an assessment of a full quantitative pharmacology model that accounts for drug disposition into the peripheral compartment.

✉ Eduardo D. Sontag
sontag@sontaglab.org

1   Department of Electrical and Computer Engineering, Northeastern University, Boston, MA, USA

2   Quantitative Pharmacology, EMD Serono Inc, Merck KGaA, Billerica, Massachusetts, USA

3   Department of Bioengineering, Northeastern University, Boston, MA, USA

4   LIX, CNRS, École Polytechnique, Institute Polytechnique de Paris, Palaiseau, France

5   Laboratory of Systems Pharmacology, Harvard Medical School, Boston, MA, USA

Springer

1 Introduction

Cancer immunotherapy has revolutionized the field of cancer treatment, highlighting that the immune system can eliminate tumors in many cases if given assistance Mellman et al. (2011). Immunotherapy approaches include reactivating immune cells through checkpoint inhibition Goleva (2021), as well as through exogenous immune cell therapies such as using Chimeric Antigen Receptor T (CAR-T) cells Feins (2019). Despite these advances, only a subset of cancers responds to these therapies ("hot" tumors), with some tumors remaining "cold", possibly because of reduced immune infiltration or lack of effective antigen presentation in the TME Bonaventura (2019); Liu and Sun (2021).

One approach to circumvent this issue is to bypass antigen presentation altogether, connecting a therapeutic agent directly with a tumor cell, a strategy implemented using bispecific T cell engagers, or TCEs Stieglmaier et al. (2015); Yuraszeck et al. (2017); Betts and van der Graaf (2020); Tian (2021). This therapeutic modality has been proposed for treating acute myeloid leukemia Laszlo (2014), multiple myeloma Hipp (2017), lymphoblastic leukemia Topp (2014), and refractory solid tumors Kebenko (2018). TCE is a promising *platform* for targeted therapy across different tumor types Einsele (2020). A list of TCE molecules that were considered in this study is presented in Table 1. A more detailed review of the existing TCEs can be found in Tian (2021); Morcos (2021).

In this study, the first objective is to evaluate the design characteristics of existing TCEs based on the simple model presented in Figure 1. The TCE drug, X, targets receptors on immune cells, T_1, which for TCEs is often CD3 or CD28 Drake (2020); Zhang (2021), and receptors on cancer cells, T_2. The drug can bind reversibly to either target, forming X-T_1 dimer D_1 at a rate constant k_{on_1} and dissociating at a rate constant k_{off_1}, or forming the X-T_2 dimer D_2 at a rate constant k_{on_2} and dissociating at a rate constant k_{off_2}. Finally, when either of the dimers bind to the remaining free target, they can form a trimer Y, which is the T_1-X-T_2 ternary complex. We call this system, involving immune cells, drug, and cancer cells, a "three-body" system. The key objective of this study is to find binding properties for the drug X on either arm given the properties of the other two targets, in such a way as to maximize concentration of Y. A schematic diagram of this process is given in Figure 1(a).

One particular challenge with these types of drugs is that the efficacy curve for TCEs is bell-shaped, rather than the standard Emax curve. By "bell shape", we mean a nonmonotonic function with a single maximum at some intermediate concentration, whereas the Emax curve is a typical pharmacology model that is monotonic and saturable Lee (2010). A TCE drug efficacy is maximized only when the drug is bound to both targets (Figure 1(b), where Y exhibits a bell-shaped curve); dimers in this drug construct (Figure 1(b), where D_1 and D_2 exhibit an Emax curve) are not expected to exhibit efficacy. This creates an important challenge, since, while for a typical Emax curve, higher drug concentration may result in an efficacy plateau, and increase in dose
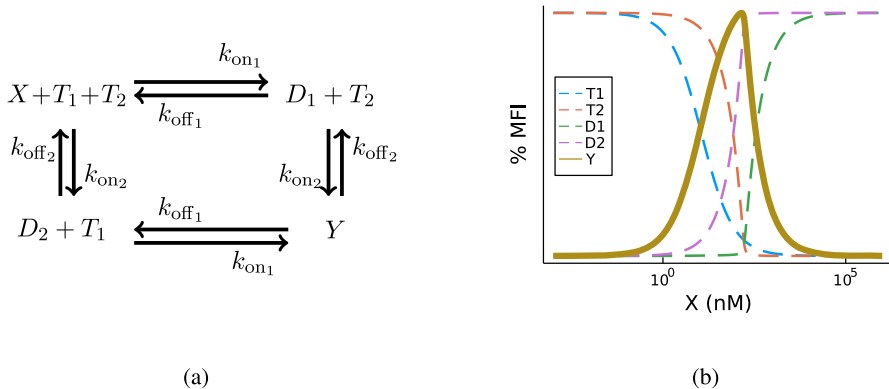
$$X + T_1 + T_2 \underset{k_{\mathrm{off}_1}}{\overset{k_{\mathrm{on}_1}}{\rightleftharpoons}} D_1 + T_2$$

(a)

(b)

Fig. 1 A schematic of the "three-body" model and the nominal *bell-shape* pattern. On the left side (a), the three-body model described in terms of TCE, where X is the drug concentration, T_1 is the target receptor expressed on immune cells, and T_2 is the target receptors expressed on cancer cells. The drug can reversibly bind to either target to form dimers D_1 and D_2 or bind to both to form trimer complex Y. Maximizing Y is expected to maximize drug efficacy. On the right side (b), a nominal bell-shape pattern of the ternary complex Y normalized to Maximum Fluorescent Intensity (MFI) at steady state is visualized as a function of initial TCE drug concentration ($X = X(0)$ in nM). Binding kinetics and initial conditions are adopted from Betts (2019). The chemical reactions are visualized in a simple form in order to provide an intuitive idea of the reactions, and the diagram does not follow the conventions of a chemical reaction network: specifically, T_2 (T_1) is not involved in the dimerization reaction between X and $T_1(T_2)$.

is mostly likely to just increase toxicity. For a bell-shaped efficacy curve (Figure 1(b), yellow thick line), increase in drug concentration will result not only in higher toxicity but also in loss of efficacy. As such, estimating maximally efficacious concentration for a TCE is significantly more challenging than for a compound with a typical Emax efficacy curve.

One of the key steps during the early stages of drug development is lead compound selection, which is based on many criteria, including drug affinity for the target, denoted as an inverse of dissociation constant K_D and defined as $K_D = \frac{k_{\mathrm{off}}}{k_{\mathrm{on}}}$, where k_{on} is the rate constant at which the drug reversibly binds to its target, and k_{off} is the dissociation rate constant. The question of affinity optimization to maximize the drug's efficacy is particularly challenging for TCEs, even those targeting similar or even the same targets. For instance, REGN5458 and REGN5459 are both targeting CD3 and BCMA receptors but with different affinities for CD3 Jordan (2020). While tighter binding (lower K_D) can be associated with achieving greater target engagement with lower drug concentration (higher potency), for TCEs and other drugs, whose efficacy is predicated on maximizing trimer concentration Y, this is not necessarily the case. Specifically, as was reported in Betts (2019); Douglass (2013), very tight binding on each arm can "take up" most of the drug, leaving less drug available to bind to the other arm, thereby decreasing the probability of trimer complex formation. Therefore, there likely exists an interplay of "optimal affinities" for both arms of the molecule, resulting in different variations of the *bell-shaped* relationship between the drug concentration and trimer complex Betts (2019).

Table 1 Existing CD3-based T Cell Engagers, sorted by the year of the referenced publication. TCEs might be engineered in different antibody structures, e.g. TCE, Half-Life Extended Bispecific T Cell Engager (HLE-TCE), and Knob-into-Holes (KIH). The targeted receptor protein of immune cells is CD3 for all the molecules considered in this study.

TCE Molecule	Target	K_{D1} (nM)	K_{D2} (nM)	Type	Structure	kDa	Ref
Blinatumomab	CD19	~ 100	~ 1	Liquid	TCE	54	Dreier (2002)
Solitomab	Ep-CAM	16 ± 12	77 ± 39	Liquid	TCE	55	Brischwein (2006)
BAY2010112	PSMA	9.4 ± 4.3	47.0 ± 8.1	Solid	TCE	55	Friedrich (2012)
PF-06671008	Pcad	11.5 ± 0.9	0.521 ± 0.162	Solid	DART	57	Root (2016)
$CD3_{\varepsilon}$ L/HER2	HER2	50	0.5	Solid	KIH	> 100	Mandikian (2018)
$CD3_{\varepsilon}$ H/HER2	HER2	0.5	0.5	Solid	KIH	> 100	Mandikian (2018)
$CD3_{\varepsilon}$ VH/HER2	HER2	0.05	0.5	Solid	KIH	> 100	Mandikian (2018)
7370	FLT3	27	49×10^{-3}	Liquid	IgG-based	146	Yeung (2020)
PF-07062119	GUCY2C	7.47 ± 0.15	23.97 ± 0.97	Solid	IgG1-FcγR	> 100	Mathur (2020)
Tarlatamab	DLL3	0.64 ± 0.05	14.9 ± 0.4	Solid	HLE-TCE	> 100	Giffin (2021)
Acapatamab	PSMA	22.4 ± 2.8	14.8 ± 2	Solid	HLE-TCE	> 100	Deegen (2021)
Anti-CD79b/CD3	CD79b	12.8	1	Liquid	KIH	150	Yadav (2022)

Four parameters are critical to characterize such a bell-shape curve at the site of action: 1) initial concentration of T_1, 2) initial concentration of T_2, 3) binding affinity/dissociation constant of the TCE to target 1 K_{D1}, and 4) dissociation constant K_{D2}. The initial concentration of T_1 depends on the number of T cells in the body. Most of the existing TCEs bind to CD3 (see Table 1), and the average turnover parameters for this particular target are relatively well understood De Boer and Perelson (2013). The initial concentration of T_2 depends on the tumor and can vary dramatically. A review of existing CD3-based TCEs, summarized in Table 1, showed that the initial concentration of tumor-specific targets is generally considered to be less than 5×10^3/cell; this however can vary across different cancer types.

The most desirable targets on cancer cells are minimally expressed in normal cells, so as to minimize off-target effects.

The affinity of the TCE molecule to T_1 (CD3 on the T cells) can be significantly smaller, comparable, or significantly larger than the binding affinity to T_2 (targeted receptor protein on the cancer cells). For example, the binding affinity of Blinatumomab Dreier (2002), PF-06671008 Root (2016), and 7370 Yeung (2020) to T_1 is lower than their affinity to T_2. The affinity of Acapatamab Deegen (2021), Solitomab Brischwein (2006), and PF-07062119 Mathur (2020) to their targets are in a comparable range. On the other hand, TCE molecules such as BAY2010112 Friedrich (2012), Taralatamab Giffin (2021), and REGN5458 Smith (2020) have a significantly higher affinity (lower dissociation constant) to T_1.

The binding kinetics of the TCE molecules with respect to each of the targets may also affect the distribution of this type of antibody in different tissues. For instance, the biodistribution of CD3/HER2 TCE, also known as T-cell-Dependent Bispecific (TDB), has been measured for different ranges of affinities to CD3 for solid tumors in mouse models Mandikian (2018), confirming the intuition that higher affinities to CD3 (lower dissociation constant K_{D1}) increase drug uptake in the peripheral tissues including lymph nodes, thereby decreasing their availability in the TME. Therefore, TCE molecules with lower affinities for CD3 are less toxic in treatments designed for solid tumors.

The characterization of the bell-shape was analytically investigated by Douglass (2013). The integration of the three-body model with the pharmacokinetics and efficacy of PF-06671008 TCE molecule was presented in Betts (2019). Here, we build on these results to create a framework to allow quantitative comparison between different TCE molecules based on their bell-shape response. We anchor the analysis to the affinity values of several existing TCE molecules, and showcase the resulting bell-shape response and its sensitivity to different parameters. We further explore the identifiability of affinity values from the experimental data, and made the connection between pharmacokinetics, efficacy and biodistribution of the TCE based on an example, where TCE molecules that target HER2 were designed to have different affinities to CD3 receptor Mandikian (2018).

In what follows, the general properties of the two targets are assumed to be known, and the focus is on approaches to identify K_D values from preclinical experiments, and on characterizing their effect on the bell-shape pattern of the concentration trimer Y at the site of action. A quantitative comparison is presented for the TCE molecules that were available in the literature at the time of this writing. The computational

analysis was performed for different scenarios, including varying ratios between target concentrations to quantify the sensitivity of projected efficacy (here correlated with maximizing the concentration of trimer Y) to initial conditions. The paper concludes with the formulation of a full quantitative pharmacology model that should facilitate a broader discussion of biodistribution of TCE molecules.

2 Methods

2.1 Three-body model

The initial process of lead compound selection is based on *in vitro* experiments, where cells are co-incubated with the drug in order to evaluate their relative affinities and where drug clearance does not affect the dynamics. Consequently, one can initially focus on just the nearly instantaneous formation of drug-target dimers and trimers, which can be interpreted as a three-body model. In recent investigations such as Betts (2019) it has been emphasized that the efficacy of the TCE drug trimer concentration at the site of action is a bell-shaped function. A too low or too high concentration of a TCE does not lead to formation of a sufficient number of trimer complexes: at low concentrations, too few trimers are formed, while at high concentrations the equilibrium shifts towards increased formation of dimers D_1 and D_2 and away from trimers. There exist, therefore, a "sweed spot" that maximizes trimer formation and consequently the expected efficacy.

A "three-body model" in the terminology of Douglass (2013) is what all bispecific antibodies have in common. In the three-body model, a bispecific antibody (binding species) connects to two different target molecules (terminal species) to form a ternary complex. After the formation of dimers between the first target and the antibody, the binding kinetics can be changed based on a cooperativity factor to increase/decrease the binding affinity of the antibody molecule of the formed dimer to the second target. A positive cooperativity can be interpreted as avidity Rhoden et al. (2016); Sengers (2016); Harms (2014); Kaufman and Jain (1992), where the apparent affinity to the second target is greater once the drug has been bound to the first target, given that both targets are expressed on the same cell surface. The cooperativity factor can be neglected in models of bispecific antibodies that target receptors on two different cell types, such as TCEs.

As mentioned above, the model described in Figure 1 includes six state variables to describe the concentrations of the TCE $X(t)$, the target receptor on the surface of the immune cells $T_1(t)$, the target receptor on the surface of cancer cells $T_2(t)$, the dimer complex of immune cell-antibody $D_1(t)$, the dimer complex of antibody-immune cell $D_2(t)$, and the ternary complex of immune cell-antibody-cancer cell $Y(t)$. The initial concentration of the dimer and trimer complexes are assumed to be zero at the starting point $D_1(0) = D_2(0) = Y(0) = 0$. The initial concentration of the TCE $X(0)$ is the concentration that is going to be assessed in subsequent analysis. The system of Ordinary Differential Equations (ODEs) describing the dynamics of these six variables
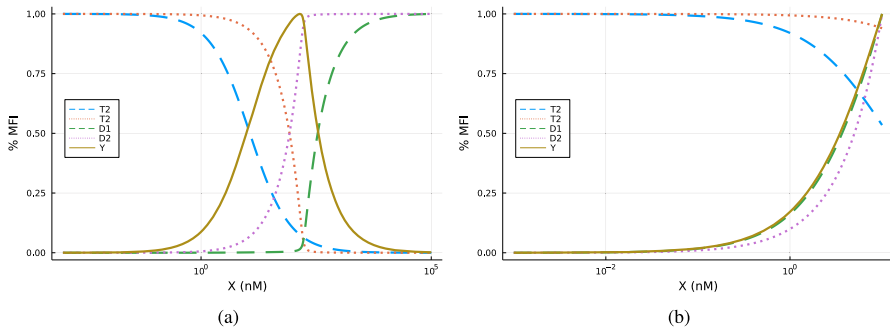
Fig. 2 Model-based steady state simulations of the three-body model (1). The vertical axis is normalized to % MFI, which represents relative fluorescence intensity normalized to the maximum observed value in a hypothetical experiment. This figure does not represent experimental data, but rather simulations using the model under two different TCE concentration ranges. These simulations illustrate that if one were to conduct experiments using different concentration ranges, they might observe distinctive patterns such as those shown here, even if the underlying biological processes are consistent. The variables in the simulations have different ranges of initial concentration of the TCE. The initial TCE concentration range and the range of horizontal axis values in (a) are larger than in (b). The plots on the left show the concentrations of the trimer and the targets, and the plots on the right side show the drug-target dimer concentrations.

is as follows:

$$\dot{X} = -k_{\mathrm{on}_1} T_1 X - k_{\mathrm{on}_2} T_2 X + k_{\mathrm{off}_1} D_1 + k_{\mathrm{off}_2} D_2, \tag{1a}$$

$$\dot{T}_1 = -k_{\mathrm{on}_1} T_1 X + k_{\mathrm{off}_1} D_1 - k_{\mathrm{on}_1} T_1 D_2 + k_{\mathrm{off}_1} Y, \tag{1b}$$

$$\dot{T}_2 = -k_{\mathrm{on}_2} T_2 X + k_{\mathrm{off}_2} D_2 - k_{\mathrm{on}_2} T_2 D_1 + k_{\mathrm{off}_2} Y, \tag{1c}$$

$$\dot{D}_1 = k_{\mathrm{on}_1} T_1 X - k_{\mathrm{off}_1} D_1 - k_{\mathrm{on}_2} T_2 D_1 + k_{\mathrm{off}_2} Y, \tag{1d}$$

$$\dot{D}_2 = k_{\mathrm{on}_2} T_2 X - k_{\mathrm{off}_2} D_2 - k_{\mathrm{on}_1} T_1 D_2 + k_{\mathrm{off}_1} Y, \tag{1e}$$

$$\dot{Y} = k_{\mathrm{on}_1} T_1 D_2 + k_{\mathrm{on}_2} T_2 D_1 - (k_{\mathrm{off}_1} + k_{\mathrm{off}_2}) Y. \tag{1f}$$

Note that the time dependence of the state variables is dropped for writing simplicity. The dot sign on top of each state variable on the left side represents the time derivative.

Model 1 contains four parameters: $k_{\mathrm{on}_1}, k_{\mathrm{off}_1}, k_{\mathrm{on}_2}$, and k_{off_2}. However, in preclinical measurements, using for example surface resonance experiments, one only estimates the dissociation constants of the two binding sites:

$$K_{D1} = k_{\mathrm{off}_1}/k_{\mathrm{on}_1}, \tag{2a}$$

$$K_{D2} = k_{\mathrm{off}_2}/k_{\mathrm{on}_2}. \tag{2b}$$

The dissociation constants K_D are sufficient to estimate the equilibrium concentration of each species in a dimerization reaction (for example $a + b \underset{k_{\mathrm{off}}}{\overset{k_{\mathrm{on}}}{\rightleftharpoons}} ab$), and different values of ($k_{\mathrm{on}}, k_{\mathrm{off}}$) that result in the same dissociation constant can change the reaction rate but do not affect the equilibrium concentrations.

The steady state reached when performing a long-time simulation of the three-body model (1) will predict the actual equilibrium concentrations, which can be thought of

as an *in silico* equivalent of an *in vitro* dose-response experiment used to estimate projected target occupancy as a function of drug concentration. Figure 2 shows a numerical simulation of the system, with corresponding parameter values listed in Table 2, representing the PF-006671008 molecule Betts (2019), and a total simulation duration of 1000 hours. The y-axis in Figures 2a and 2b is normalized to capture % of Maximum Fluorescence Intensity (MFI), where MFI represents fluorescence intensity normalized to the maximum observed value in a given experiment. Because the normalization depends on the tested concentration range, MFI-based results may appear different across experiments even if the underlying biological response is similar. The relative concentrations are measured based on the relative strength of the fluorescent signal. Analyzing the factors that affect the characteristic bell shape of the projected trimer concentration is the focus of this section. Picking the "right" range of molecule concentrations is critical in visualization of the bell shape. For example, note when comparing Figure 2a and Figure 2b, how different experimental results might look when reported in MFI format with different ranges of drug concentration on the x-axis.

2.2 The bell-shaped response

We have investigated the sensitivity of the bell-shaped response peak, to the binding kinetics of the TCE molecule at the site of action, here in the TME, and the initial concentration of each target. The maximum concentration (peak) of the trimer complex Y and the corresponding initial TCE concentration that results in maximum trimer concentration (optimal TCE) are the main outputs of interest in this analysis. We used the three-body portion of the quantitative model published for PF-06671008 TCE molecule Betts (2019), as an example, to assess the sensitivity of the peak of the bell-shape by changing each of the parameters in model (1), while keeping the other parameters of the model constant.

2.3 Comparison between TCEs

The three-body model (1) was used as a tool to quantitatively compare existing CD3-based TCEs summarized in Table 1 based on their published binding kinetics to their targets. The molecules included in this study are divided into two general categories: targeting solid tumors and targeting liquid tumors. Although each of the molecules might have different structures, biodistribution, metabolism, or pharmacokinetic characteristics, the three-body model captures the general structure of the interactions of these compounds with their targets at the site of action.

Numerical simulations were conducted assuming initial target concentrations of 0.108 nM and 166 nM (based on Betts (2019)). Due to the lack of reported association (k_{on}) and dissociation (k_{off}) rate constants for all molecules, k_{on} was fixed to 1 nM^{-1} h^{-1}, and k_{off} was inferred from the published equilibrium dissociation constant (K_D × 1 nM^{-1} h^{-1}) values listed in Table 1.

2.4 Biodistribution

A full dynamic model for biodistribution of the TCE molecules in humans with IV dosing is shown in Equations (3). This is a modified version of the model presented in Betts (2019), where the number of tumor-related compartments is reduced to two for simplicity, and all the immune system tissues such as lymph nodes are lumped into a single additional compartment. We use this model to obtain a better mechanistic understanding of the relationship between dissociation kinetics and biodistribution.

The differences between model (3) and the model presented in Betts (2019) are as follows: 1) an extra compartment is included in order to represent tissues with a higher concentration of immune cells, e.g. lymph nodes, 2) intermediate compartments are integrated into the main tumor compartment, and 3) biodistribution depends on the affinity of the TCE molecule to different targets, which could be explained by the flow of the immune cells between lymph nodes and the central compartment. The additional parameters included in this model are not fit to data, and the presented parameters are chosen arbitrarily based on numerical simulations to demonstrate the quantitative approach for explaining the biodistribution of the TCE molecules. Molecule and target-specific parameters can be used as needed provided data availability.

The relative change of the target concentration is assumed to be negligible in comparison with the distribution rate constants of the TCE in the present model. Moreover, the rate constant of target 1 is assumed to be faster between the central compartment and the lymph nodes (k_{lcT} and k_{clT}) relative to the rate constant of the target 1 between the central compartment and the TME (k_{ctT} and k_{tcT}). The rate constants of the TCE between the central compartment and the lymph nodes (k_{lc} and k_{cl}) are assumed to be slower than the rate constants of target 1 (k_{lcT} and k_{clT}). The reason is the increased flow rate of immune cells between lymph nodes and the central compartment.

$$\dot{X}_c = \rho u(t) - k_{el_X} X_c - k_{cp} X_c + k_{pc} X_p \frac{V_p}{V_c} - k_{cl} X_c - k_{lc} X_l \frac{V_l}{V_c}$$
$$- k_{on_1} X_c T1_c + k_{off_1} D1_c - k_{on_2} C_c T2_c$$
$$+ k_{off_2} D2_c - k_{td}(X_c - \frac{X_t}{k_\varepsilon})\frac{M_1 + M_2}{w V_c}, \tag{3a}$$

$$\dot{X}_p = k_{cp} X_c \frac{V_c}{V_p} - k_{pc} X_p, \tag{3b}$$

$$\dot{X}_l = k_{cl} \frac{X_c}{\alpha K_{D1} + \beta} \frac{V_c}{V_l} - k_{lc} X_l, \tag{3c}$$

$$\dot{T1}_l = k_{synT} - k_{clT} T1_c \frac{V_c}{V_l} + k_{lcT} T1_l - k_{on_1} X_l T1_l + k_{off_1} D1_l, \tag{3d}$$

$$\dot{D1}_l = k_{on_1} X_l T1_l - k_{off_1} D1_l, \tag{3e}$$

$$\dot{T1}_c = -k_{ctT} T1_c + k_{tcT} T1_t \frac{M_1 + M_2}{w V_c} - k_{on_1} X_c T1_c + k_{off_1} D1_c - k_{elT} T1_c, \tag{3f}$$

$$\dot{D1}_c = k_{on_1} X_c T1_c - k_{off_1} D1_c, \tag{3g}$$

$$\dot{T2}_c = k_{syn} - k_{deg} T2_c - k_{on_2} X_c T2_c + k_{off_2} D2_c, \tag{3h}$$

$$\dot{D2_c} = -k_{elD}D2_c + k_{on_2}X_cT2_c - k_{off_2}D2_c, \tag{3i}$$

$$\dot{X_t} = k_{td}(X_c - \frac{X_t}{k_\varepsilon}) - k_{on_1}T1_tX_t - k_{on_2}T2_tX_t + k_{off_1}D1_t + k_{off_2}D2_t, \tag{3j}$$

$$\dot{T1_t} = k_{ctT}T1_c\frac{wV_c}{M_1+M_2} - k_{tcT}T1_t - k_{on_1}T1_tC_t + k_{off_1}D1_t$$
$$- k_{on_1}T1_tD2_t + k_{off_1}Y, \tag{3k}$$

$$\dot{T2_t} = -k_{on_2}T2_tC_t + k_{off_2}D2_t - k_{on_2}T2_tD1_t + k_{off_2}Y, \tag{3l}$$

$$\dot{D1_t} = k_{on_1}T1_tC_t - k_{off_1}D1_t - k_{on_2}T2_tD1_t + k_{off_2}Y, \tag{3m}$$

$$\dot{D2_t} = k_{on_2}T2_tC_t - k_{off_2}D2_t - k_{on_1}T1_tD2_t + k_{off_1}Y, \tag{3n}$$

$$\dot{Y} = k_{on_1}T1_tD2_t + k_{on_2}T2_tD1_t - (k_{off_1} + k_{off_2})Y, \tag{3o}$$

$$\dot{M_1} = \frac{k_{ge}M_1(1 - \frac{M_1+M_2}{k_v})}{(1 + (\frac{k_{ge}}{k_{gl}}(M_1+M_2))^{k_\psi})^{1/k_\psi}} - \frac{k_{max} \times Y}{kc_{50} + Y}M_1, \tag{3p}$$

$$\dot{M_2} = \frac{k_{max} \times Y}{kc_{50} + Y}M_1 - M_2/k_\tau. \tag{3q}$$

In these equations, X is the concentration of drug, T is the concentration of targets, D is the drug-target dimer concentration, Y is the trimer concentration, and M is the tumor volume intermediate compartment. All parameters and variables are defined in detail in Tables 2 and 3. The dot sign on top of the variables is a time derivative $\dot{f}(t) = \frac{df(t)}{dt}$.

2.5 Identifiability

The goal of performing identifiability analysis is to assess whether model parameters could be uniquely recovered from experiments. In this paper we will discuss two different setups for identifiability: 1) identification of the K_D values from time course data, and 2) identification of K_D values from steady state data. Time course data plays a major role in the drug development process for *in vivo* studies, and steady state data is often used for *in vitro* studies to assess potential drug efficacy. Notably, this analysis is based on deterministic data and should be treated as a proof-of-concept approach to recover K_D values from specific experiments.

The standard context for performing identifiability analysis is for the case when the parameter values are to be inferred from time course data for some measured quantities Miao (2011). In this case, one typically considers an ODE model in the state-space form

$$\dot{\mathbf{x}} = \mathbf{f}(\mathbf{k},\mathbf{x}) \quad \text{and} \quad \mathbf{y} = \mathbf{g}(\mathbf{k},\mathbf{x}), \tag{4}$$

where $\mathbf{x}$ and $\mathbf{y}$ are the vectors of states and observed quantities, respectively, and $\mathbf{k}$ is a vector of scalar parameters. For the three-body model (1), we would have $\mathbf{x} = [X, T_1, T_2, D_1, D_2, Y]^T$, the observed quantities would be $y_1 = X$, $y_2 =$

Table 2 Parameters used in model (3), are based on previously published parameters Betts (2019); parameters different from Betts (2019) are marked by asterisk.

	Value	Unit	Definition
V_c	40.2	mL/kg	Volume of distribution in the central compartment
V_p	211	mL/kg	Volume of distribution in the peripheral compartment
V_l^*	92	mL/kg	Volume of distribution in the lymph compartment
k_{el_X}	1.16×10^{-1}	1/h	Clearance in the central compartment
k_{el_T}	2.51	1/day	Elimination rate of immune cells (Target 1)
k_{cp}	6.27×10^{-1}	1/h	Redistribution rate constant to the peripheral compartment
k_{pc}	1.19×10^{-1}	1/h	Redistribution rate constant to the central compartment
$k_{cl_T}^*$	1×10^{-1}	1/day	Target 1 redistribution to the lymph nodes
α	1	1/nM	Empirical parameter
β	5	1	Empirical parameter
$k_{lc_T}^*$	5×10^{-1}	1/day	Target 1 redistribution to the central from lymph
k_{cl}^*	5×10^{-2}	1/day	Redistribution rate constant to the lymph compartment
k_{on_1}	1.72	1/nM/h	Binding of the antibody and target 1
k_{off_1}	19.66	1/h	Unbinding rate of the antibody-target 2 dimer
k_{on_2}	1.57	1/nM/h	Binding rate of the antibody and target 2
k_{off_2}	0.74	1/h	Unbinding rate of the antibody-target 2 dimer
k_{deg}	1.5×10^{-1}	1/h	Tumor $T2_c$ degradation rate constant
k_{syn}	$k_{deg} \times T2_c(0)$	nM/h	Tumor synthesis rate constant
k_{synT}	$k_{elT} \times \frac{T1_c(0)V_l}{V_c}$	nM/h	Synthesis rate of the immune cells (no proliferation)
k_{td}	1.082	1/h	Disposition rate to the TME (depends on tumor physiology Thurber and Wittrup (2012))
k_{ctT}	2×10^{-3}	1/day	T cell redistribution from the central to the TME
k_{tcT}	5×10^{-4}	1/day	T cell redistribution from the TME.
k_{max}	1.32	1/day	Maximum killing rate
kc_{50}	6.9×10^{-5}	nM	Concentration at half maximum
k_{ge}	1.9×10^{-1}	1/day	Exponential tumor growth rate

Table 2 continued

	Value	Unit	Definition
k_{gl}	1.23×10^{-1}	mL/day	Linear tumor growth rate
k_v	6.0	mL	Maximum tumor volume
k_τ	3.99	day	Transduction time between tumor compartments.
k_ψ	20	1	Exponential to linear transition rate of the tumor
w	80	kg	Weight of a patient.
ρ	9.52	nM/(μg/kg)	Concentration unit conversion for in the central compartment

Table 3 Variables used in model (3).

Variable	Unit	Initial value	Definition
u	mg/kg/day	-	Input: drug dose.
X_c	nM	0.0	Antibody concentration in central compartment.
X_l	nM	0.0	Antibody concentration in immune system tissue.
X_p	nM	0.0	Antibody concentrations in peripheral compartment.
X_t	nM	0.0	Antibody concentrations in the TME.
$T1_l$	nM	5.0	Target 1 concentration in the immune system tissue.
$T1_c$	nM	0.83	Target 1 concentration in the central compartment.
$T1_t$	nM	1.08×10^{-1}	Target 1 concentration in the TME.
$T2_c$	nM	1.1	Target 2 concentration in the central compartment.
$T2_t$	nM	1.66×10^2	Target 2 concentration in the TME.
$D1_l$	nM	0.0	Dimer drug-target 1 in the immune system tissue.
$D1_c$	nM	0.0	Dimer drug-target 1 in the central compartment.
$D1_t$	nM	0.0	Dimer drug-target 1 in the TME.
$D2_c$	nM	0.0	Dimer drug-target 2 in the central compartment.
$D2_t$	nM	0.0	Dimer drug-target 2 in the TME.
Y	nM	0.0	Trimer concentration in the TME.
$M1$	mL	1.0	Tumor volume in growth compartment.
$M2$	mL	0.0	Tumor transduction compartment.

T_1, $y_3 = T_2$ (free drug, first target, and second target, respectively), and $\mathbf{k} = [k_{\text{on}_1}, k_{\text{on}_2}, k_{\text{off}_1}, k_{\text{off}_2}]^T$.

For a model (4), a function $h(\mathbf{k})$ of parameters (could be just a parameter) can be

- *globally identifiable* if, for almost every solution of (4), any other solution of (4) with the same trajectory for $\mathbf{y}$ must have the same value of $h(\mathbf{k})$.
- *locally identifiable* if, for almost every solution of (4), there are finitely many possible values of $h(\mathbf{k})$ for any other solution of (4) with the same trajectory for $\mathbf{y}$;
- *nonidentifiable* if, for almost every solution of (4), there are infinitely many possible values of $h(\mathbf{k})$ for other solutions of (4) with the same trajectory for $\mathbf{y}$.

Let us elaborate on the notion of "almost every" in the above definitions. Every trajectory of (4) is uniquely determined by a pair $(\mathbf{k}, \mathbf{x}(0))$ of the parameter vectors and initial conditions. Then "almost every" means that that there exists a manifold of codimension at least one (and, thus, of Lebesque measure zero) in this $(\mathbf{k}, \mathbf{x}(0))$-space such that the stated property may fail only for the trajectories from this manifold. For a more precise formalization of this notion and related discussions, we refer to (Hong (2020), Section 2). Note that a globally identifiable parameter is locally identifiable as well. The term "*generic*" (global or local) identifiability is sometimes used in order to emphasize that there is a possible exceptional set in which identifiability does not hold. We will give two simple examples to illustrate these notions.

Example 1 Consider a model $\dot{x} = k_1 k_2 x$ with the observable $y = x$. Then the trajectories are of the form $x(t) = x_0 e^{k_1 k_2 t}$. We can see that neither k_1 nor k_2 is identifiable because the same trajectory can be produced by infinitely many triples $(k_1/c, k_2 c, x(0))$, where c ranges over nonzero numbers. On the other hand, take the function $h(\mathbf{k}) = k_1 k_2$. Consider the manifold consisting of all pairs of the form $(\mathbf{k}, 0)$, that is, pairs of parameter vectors and the special initial state $x(0) = 0$. For every solution not starting from this manifold, we have identifiability. Indeed, if $x_0 e^{k_1 k_2 t} = x_0 e^{k_1' k_2' t}$ for all t, and $x_0 \neq 0$, then $k_1 k_2 = k_1' k_2'$. Thus, $h(\mathbf{k})$ is globally identifiable.

Example 2 Consider a model $\dot{x} = -kx$ with the observable $y = x$. Then the trajectories are of the form $x(t) = x_0 e^{-kt}$. If $x(0) \neq 0$, the growth rate k is uniquely defined by the function $y(t)$ via, for example, a formula $k = \frac{\dot{y}(0)}{y(0)}$. If $x(0) = 0$, then all values of k yield the same $y(t) = 0$.

We claim that in this model k is globally identifiable. Indeed, the trajectories not allowing for unique reconstruction of k (namely, the trajectories with $x(t) = 0$) correspond to a codimension one subvariety $(k, 0)$ in the $(k, x(0))$-space parametrizing all the trajectories.

There are a number of software tools for assessing identifiability Barreiro and Villaverde (2023) using the time course data. We have chosen to use the web-based Structural Identifiability Analyzer Ilmer et al. (2021) , which is based on the algorithms from Hong (2019); Ovchinnikov (2021). This algorithm takes as input a model in the format (4)[1]. For the three-body model (1), the software showed that all four parameters k_{on_1}, k_{on_2}, k_{off_1}, k_{off_2} are globally identifiable from the time course data.

---

[1] The three-body model (1) in the required format can be found in the github repository at https://github.com/mahdiarsadeghi/tce/blob/main/identifiability/00_time_course.md

While the time course identifiability results presented above are of mathematical interest, they are not the most useful in our context, because most experimental measurements are typically done at steady state Dreier (2002); Brischwein (2006); Friedrich (2012); Root (2016); Yeung (2020); Mathur (2020); Giffin (2021); Deegen (2021). Thus, we next turn our attention to the more interesting question of identification on the basis of steady state data alone.

In this setup, we fix a subset $\mathcal{T}$ in the $(\mathbf{k}, \mathbf{x}(0))$-space of the considered trajectories (e.g., trajectories with positive parameter values and nonnegative initial conditions). For the problem to be well-posed, it is necessary that every trajectory in $\mathcal{T}$ converges to a steady state. For $(\mathbf{k}, \mathbf{x}(0)) \in \mathcal{T}$, we will denote the corresponding steady state by $\mathcal{S}(\mathbf{k}, \mathbf{x}(0))$. Then we will call a function $h(\mathbf{k})$ globally identifiable from the steady state data if there exists a subset $\mathcal{T}_0 \subset \mathcal{T}$ of Lebesque measure zero such that

$$\forall(\hat{\mathbf{h}}, \hat{\mathbf{x}}(0)) \in \mathcal{T} \setminus \mathcal{T}_0, \ (\tilde{\mathbf{h}}, \tilde{\mathbf{x}}(0)) \in \mathcal{T}: \quad \mathbf{y}(\mathcal{S}(\hat{\mathbf{k}}, \hat{\mathbf{x}}(0)))$$
$$= \mathbf{y}(\mathcal{S}(\tilde{\mathbf{k}}, \tilde{\mathbf{x}}(0))) \implies h(\hat{\mathbf{k}}) = h(\tilde{\mathbf{k}}).$$

We perform a detailed analysis of the three-body model in this setup in Section 3.4, and here we give illustrative examples explaining the steady state setting and its differences from the time course identifiability.

Example 3 We revisit Example 2 with the model $\dot{x} = -kx$, and set $\mathcal{T}$ to be trajectories with positive k. Then, for any initial condition, there is a unique attracting steady state $\mathcal{S}(k, x(0)) = 0$. Assume that what is measured is precisely this steady state. Since the steady state is zero regardless of the value of k, the parameter k is not identifiable from the steady state data (unlike the time course setting of Example 2).

Example 4 Consider the model of logistic growth $\dot{x} = x(k - x)$ with $y = x$ and $\mathcal{T}$ being the set of $(k, x(0))$ with $k > 0$ and $x(0) \geqslant 0$. It is well-known that, if $x(0) > 0$, there is a unique attracting steady state $\mathcal{S}(k, x(0)) = k$. Furthermore, we have $\mathcal{S}(k, 0) = 0$. Therefore, the knowledge of the steady state is sufficient to find the value of k if $x(0) > 0$. Thus, by setting $\mathcal{T}_0 = \{(k, x(0)) \in \mathcal{T} \mid x(0) = 0\}$, we see that k is globally identifiable.

The next example can serve as a toy model for the analysis of the three-body problem we will perform in Section 3.4.

Example 5 Consider the following chemical reaction network with three species X_1, X_2, X_3:

$$X_1 + X_2 \underset{k_1}{\overset{k_2}{\rightleftharpoons}} X_3,$$
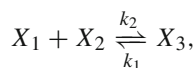
which, under the law of mass-action kinetics, is governed by the following ODE system (x_i denotes the concentration of X_i for $i = 1, 2, 3$):

$$\dot{x}_1 = k_1 x_3 - k_2 x_1 x_2, \quad \dot{x}_2 = k_1 x_3 - k_2 x_1 x_2, \quad \dot{x}_3 = -k_1 x_3 + k_2 x_1 x_2. \tag{5}$$

We will consider the set $\mathcal{T}$ of trajectories with positive parameter values and $x_1(0) = c_1 > 0$, $x_2(0) = c_2 > 0$, $x_3(0) = 0$. It is known Sontag (2001) that every such trajectory converges to a steady state. We assume that the measured quantities are the values of x_2 and x_3 at the steady state, that is, $\mathbf{y} = [x_2, x_3]^T$, and we are interested in identifiability of $K = \frac{k_1}{k_2}$.

If (x_1^*, x_2^*, x_3^*) are the coordinates of the steady state, then they satisfy the equation

$$0 = K x_3^* - x_1^* x_2^* = K x_3^* - (c_1 - x_3^*) x_2^*.$$

The equation contains two unknown values, K and c_1, so we cannot find the value of K using only this information.

Assume now that we can perform two independent experiments with the same (but still unknown) value of c_1 and different values of c_2, we will denote them $c_2^{[1]}$ and $c_2^{[2]}$. Formally, we have model consisting of two copies of (5) and the set of trajectories

$$\mathcal{T} = \{(\mathbf{k}, \mathbf{x}^{[1]}(0), \mathbf{x}^{[2]}(0)) \mid \mathbf{k}, x_2^{[1]}(0), x_2^{[2]}(0) > 0, \ x_1^{[1]}(0)$$
$$= x_1^{[2]}(0) > 0, \ x_3^{[1]}(0) = x_3^{[2]}(0) = 0\}.$$

We denote the coordinates of the steady states by $(x_1^{[i]}, x_2^{[i]}, x_3^{[i]})$ for $i = 1, 2$. In this case we get a system of two equations:

$$0 = K x_3^{[i]} - c_1 x_2^{[i]} + x_2^{[i]} x_3^{[i]}, \qquad \text{for } i = 1, 2.$$

Regarding this system as a linear system in the unknowns c_1 and K, we can use Cramer's rule to eliminate c_1 and get a formula for K (this elimination task becomes more tedious in higher dimensions, so we will employ Gröbner bases to do this in Section 3.4):

$$K = \frac{x_2^{[1]} x_2^{[2]} (x_3^{[1]} - x_3^{[2]})}{x_3^{[1]} x_2^{[2]} - x_3^{[2]} x_2^{[1]}}. \tag{6}$$

The formula above is well-defined as long as $\frac{x_3^{[1]}}{x_2^{[1]}} \neq \frac{x_3^{[2]}}{x_2^{[2]}}$. The value of $\frac{x_3^*}{x_2^*}$ is completely determined by K, c_1, c_2. Furthermore, it is an algebraic function in these variables (see Sontag (2001), p. 1036). We observe that this function is nonconstant with respect to c_2 when c_1 and K are fixed. Indeed, since $x_3^* \leqslant c_1$ and $x_2^* = c_2 - x_3^* \geqslant c_2 - c_1$, the value of the function can be made arbitrarily close to zero by taking c_2 sufficiently large. Therefore, for every $K, c_1, c_2^{[1]}$, there are only finitely many values of $c_2^{[2]}$ with $\frac{x_3^{[1]}}{x_2^{[1]}} = \frac{x_3^{[2]}}{x_2^{[2]}}$. Therefore, a subset $\mathcal{T}_0$ of pairs trajectories for which $\frac{x_3^{[1]}}{x_2^{[1]}} = \frac{x_3^{[2]}}{x_2^{[2]}}$ is of measure zero inside $\mathcal{T}$. Together with (6), this proves identifiability of K. So we conclude that the value of K is identifiable from the steady state data of two experiments.

2.6 Computational resources

SIAN Hong (2019) was used for structural identifiability analysis and analytical derivations. Numerical simulations and figures are produced with the Julia programming language Bezanson (2017). The DifferentialEquations package was used for numerical calculations Rackauckas and Nie (2017), with Tsit5() numerical algorithm that is suitable for non-stiff problems. The numerical software for reproducing the figures presented in the manuscript along with more examples are publicly available on Github [48].

3 Results

3.1 Results regarding the bell-shaped response

We examined the bell-shape response using the molecule PF-06671008 TCE from Betts (2019) as an example to assess the sensitivity of the peak of the bell-shape to the K_D values between the drug and either of its two targets (see Figure 3). As one can see in the two left subfigures of Figure 3a an increase in the values of K_{D1}, and K_{D2} results in a significant decrease of the maximal value of Y. On the other hand, by looking at the right side of Figure 3a, it can be observed that the optimal concentration of TCE (the corresponding initial concentration of the TCE at the peak of the trimer concentration) will be decreased by only reducing K_{D1}, and increased by increasing either K_{D1} or K_{D2}.

The sensitivity of the maximum trimer concentration, and optimal TCE initial concentration to the initial concentration of the targets on the immune cells $T_1(0)$, and cancer cells $T_2(0)$ are visualized in one-dimensional plots of Figure 3b. From the left side, it can be observed that the maximum trimer concentration is sensitive to $T_1(0)$ and insensitive to $T_2(0)$, which is physiologically reasonable, since the initial concentration of the first target, CD3 receptors on immune cells, is much smaller relative to the second target, P-cad protein on the tumor cells. This result is consistent with the sensitivity analysis presented in Betts (2019). Surprisingly, any change above 0.01x, or below 100x in the initial concentration of the target $T_1(0)$ does not affect the predicted optimal TCE concentration but significantly changes the peak of trimer concentration Y.

The dissociation constants K_{D1} and K_{D2} depend on the TCE design, while $T_1(0)$ and $T_2(0)$ depend on the tumor characteristics and variability among cancer patients. From a design perspective, it would be ideal if the maximum trimer concentration and the corresponding TCE concentration are less sensitive to the initial concentration of the targets. From a toxicity perspective, it would be favorable if a lower concentration of TCE antibody can produce the same amount of trimer in the TME. In the analysis presented in Figure 3a, it can be observed that the concentration of TCE that results in the maximum trimer concentration can be decreased by reducing the dissociation constant of the first target K_{D1}, and also that lower K_{D1} will result in a slightly higher trimer concentration.
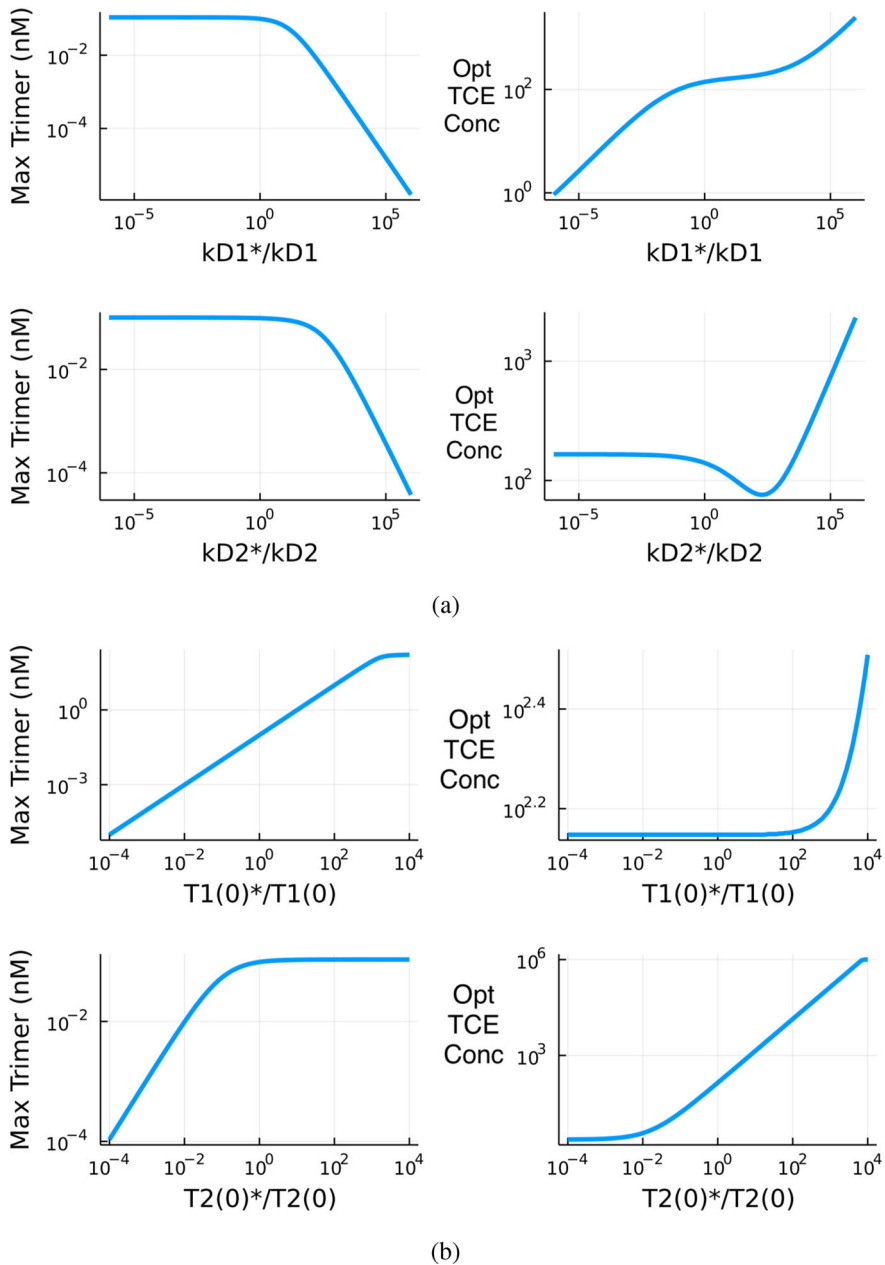
Fig. 3 Log-log plots of the bell-shape characteristics: the effects of (a) sweeping dissociation constants, and (b) sweeping target concentrations at the site of action on the peak of the trimer concentration Y and its corresponding TCE concentration X. The horizontal axes are the log scale difference between the modified parameter (marked with a star*) and their original value. Maximum trimer concentration is the peak of the bell-shape, and Optimal TCE is the corresponding initial antibody concentration, based on model (1).
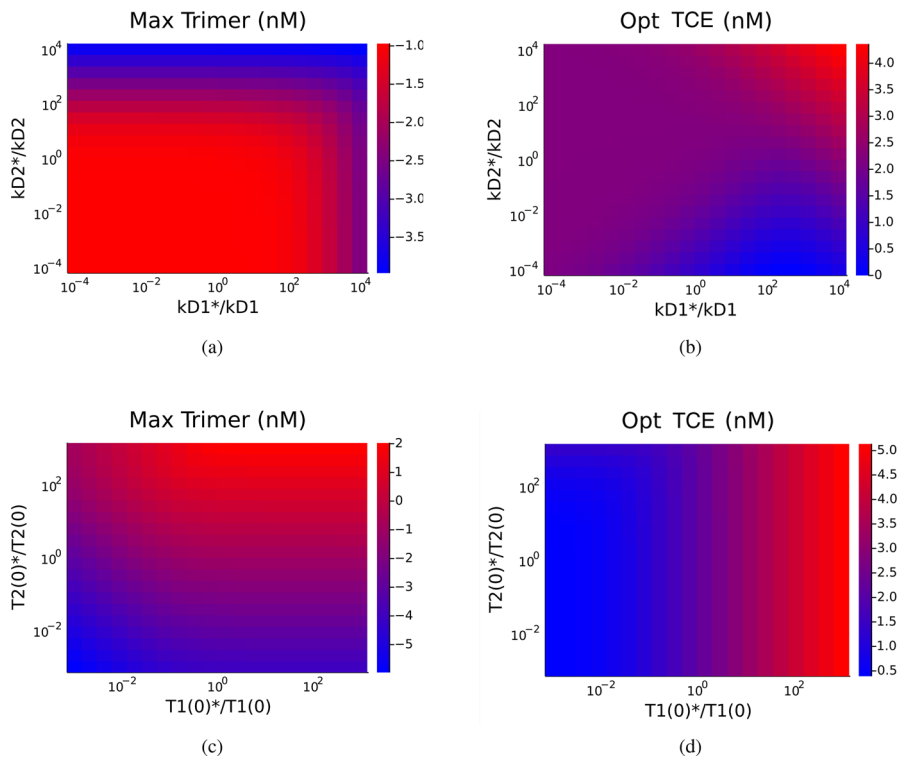
Fig. 4 Sensitivity of the bell-shape in two dimensions: Bell-shape characteristics heatmap: the effects of sweeping the TCE antibody dissociation constants, K_{D1} and K_{D2}, on (a) maximum of the trimer concentration of the bell-shape, and (b) the corresponding optimal, TCE concentration. The effect of sweeping initial target concentrations on (c) maximum of the trimer concentration of the bell-shape, and (d) the corresponding optimal concentration of the drug. The colors are plotted in log scale concentrations in nM. The horizontal and vertical axes are in log scale difference of the modified parameter (marked with a star*) and its original value, based on model (1).

Figure 4 extends the visualizations presented in Figure 3. The sensitivity of the maximum trimer concentration is on the left, and the sensitivity of the corresponding initial concentration of the TCE molecule is on the right. The red color represents a higher value of the nM concentrations in the log scale, and the blue color represents lower concentrations in the log scale. The vertical pattern in Figure 4a, and the horizontal pattern in Figure 4dare consistent with conclusions made from Figure 3. Moreover, the contrasting colors in the top left and the bottom right of Figure 4bsuggest that a simultaneous increase in dissociation constants K_{D1}, with a decrease in K_{D2}, is favorable in reducing the required TCE concentration to achieve the maximum concentration of the trimer at the site of action.

3.2 Results on comparison between TCEs

We used the three-body model (1) in order to quantitatively compare the existing CD3-based TCEs summarized in Table 1. We grouped these molecules into two general categories: those targeting solid tumors and those targeting liquid tumors. In addition to K_D values summarized in Table 1, the initial concentration of the targets is necessary for a computational study of the three-body model. As the initial concentration of target receptors is highly dependent on cancer type, the comparison between the main characteristics of the bell-shape pattern, like the trimer peak, the corresponding TCE concentration at the peak, and the width of the peak, are done for different initial concentrations of the targets to capture a variety of scenarios.

A visual comparison between the bell-shapes of the molecules considered in this study is shown in Figure 5. The ratio of the initial concentration of the targets ($T_1(0)$: $T_2(0)$) is expected to be in the range of 1:10 to 1:1000 for solid tumors (Figure 5a), and in the range of 10:1 to 1:10 for liquid tumors (Figure 5b). It can be observed that in addition to the peak of the bell-shape, and the corresponding concentration of the TCE, the width of the bell-shape varies for different ratios of the initial concentration of the targets. For instance, the width of the peak of Tarlatamab is higher for a dense tumor, where the initial concentration of the target receptors on the cancer cells is greater than the concentration of target receptors on the immune cells.

The quantitative framework used for comparing bell-shapes of the TCE molecules at different ratios of initial concentration of the targets can be extended to continuous ratios of the targets. For this purpose, the basic characteristics of bell-shape are extracted across different ratios between the targets, shown in Figure 6. The peak of the trimer concentration is the maximum of bell-shape (on top), the corresponding TCE concentration is the initial concentration of the TCE that results in the maximum of the bell-shape (in the middle), and the bell-shape width is simply the range of the TCE concentration that results in at least 50% of the maximum of the bell-shape (on the bottom).

For a realistic comparison between TCEs for solid tumors (Figure 6a), the left-hand side of the horizontal axis should be considered, where the initial concentration of target receptors on cancer cells is much greater than the initial concentration of the CD3 target receptors on immune T cells. Similarly, for a realistic comparison between TCEs designed for liquid tumors (Figure 6b), the right middle or right side of the horizontal should be taken into consideration.

3.3 Results on biodistribution

It is clear that the biodistribution of TCEs is highly dependent on the parameters given in Table 3. Note that the parameters presented here are for a nominal TCE molecule, and are not identified from a specific data set.

In addition to dissociation constants, parameters affecting drug distribution can have a critical impact on trimer maximization. These parameters are essentially the disposition rate constant of the TCE to the lymph nodes k_{cl}, and the disposition rate constant of the TCE to the TME. Notably, other parameters, such as the elimination rate
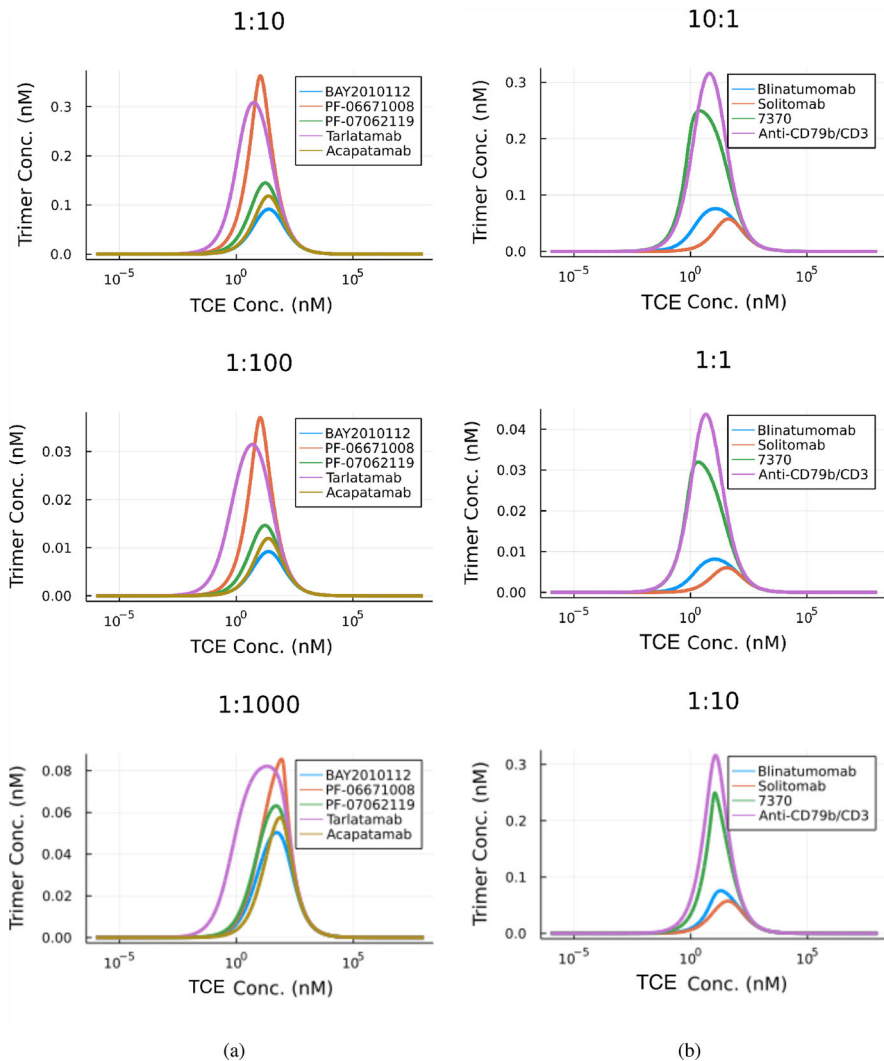
Fig. 5 Numerical comparison between the bell shapes of TCEs designed for (a) solid tumors, and (b) liquid tumors based on model (1). The relative concentration of the targets $T_1(0) : T_2(0)$ is printed on the top of each plot. The horizontal axes are in log scale, and the vertical axes are in linear scale.

(k_{el_X}) in the model, could also be affected by TCE design. Efforts to extend the TCE half-life led to the discovery of HLE-TCE molecules like Tarlatamab Giffin (2021), and Acapatamab Deegen (2021).

From the experimental results presented in Mandikian (2018), it can be observed that an increase in the affinity of the TCE toward immune cells (CD3, or target 1) increases its concentration in immune system-related tissues like lymph nodes. The mechanism of action suggests an inverse relationship between parameters k_{cl} and K_{D1}. The numerical simulation presented in Figure 7acompares two nominal TCEs
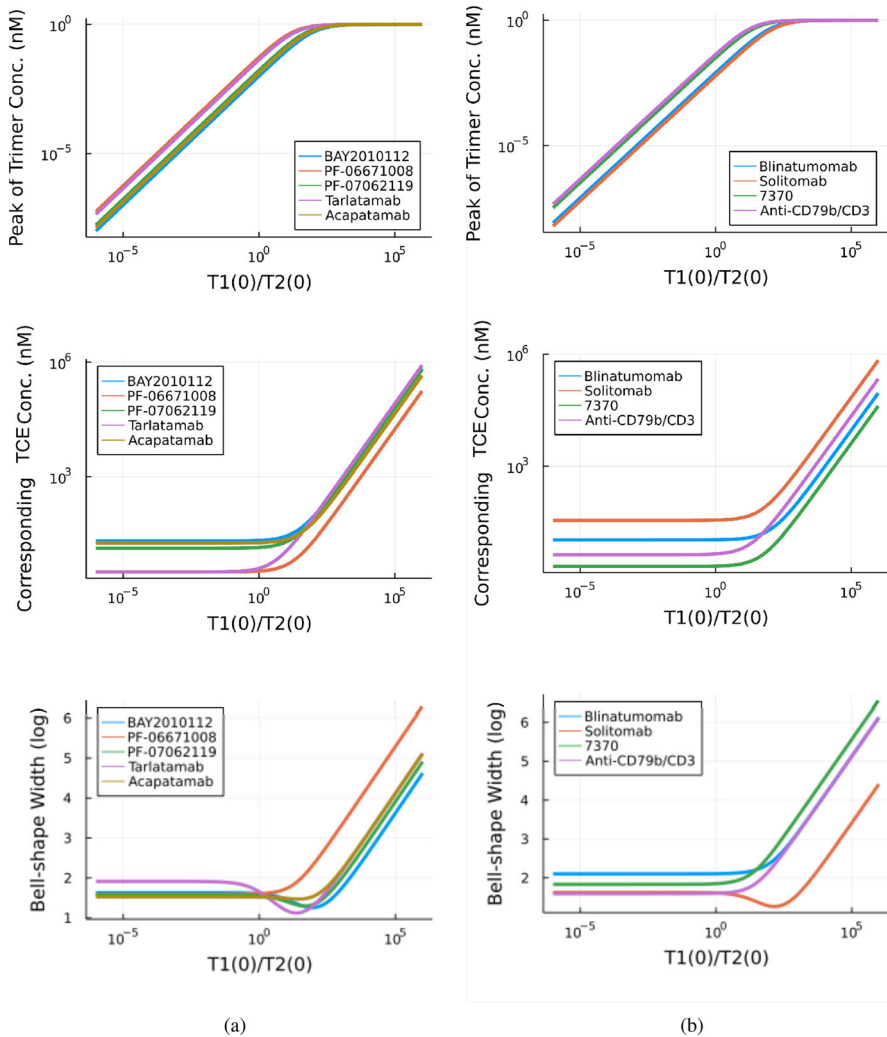
Fig. 6 Numerical comparison between the basic characteristics of the bell-shape response of different TCEs designed for (a) solid, and (b) liquid tumors based on model (1). The top figures represent the value of the peak of bell-shape, the middle figures represent the corresponding TCE antibody concentration at the peak of the bell-shape, and the bottom figures represent the width of the peak of the bell-shape. The relative initial concentration of the targets $T_1(0)/T_2(0)$ is visualized in log scale of the horizontal axes.

with different K_{D1} values administered at the same dose level. While pharmacokinetics in the central compartment X_c, and the peripheral compartment X_p are similar, the concentrations at the lymph compartment X_l are different. Furthermore, different affinities of the TCE molecule to different targets lead to a different trimer concentration in the TME, which is discussed in detail in the previous section. Model 2, with parameters and initial conditions specified in Tables 2 and 3, was used to simulate
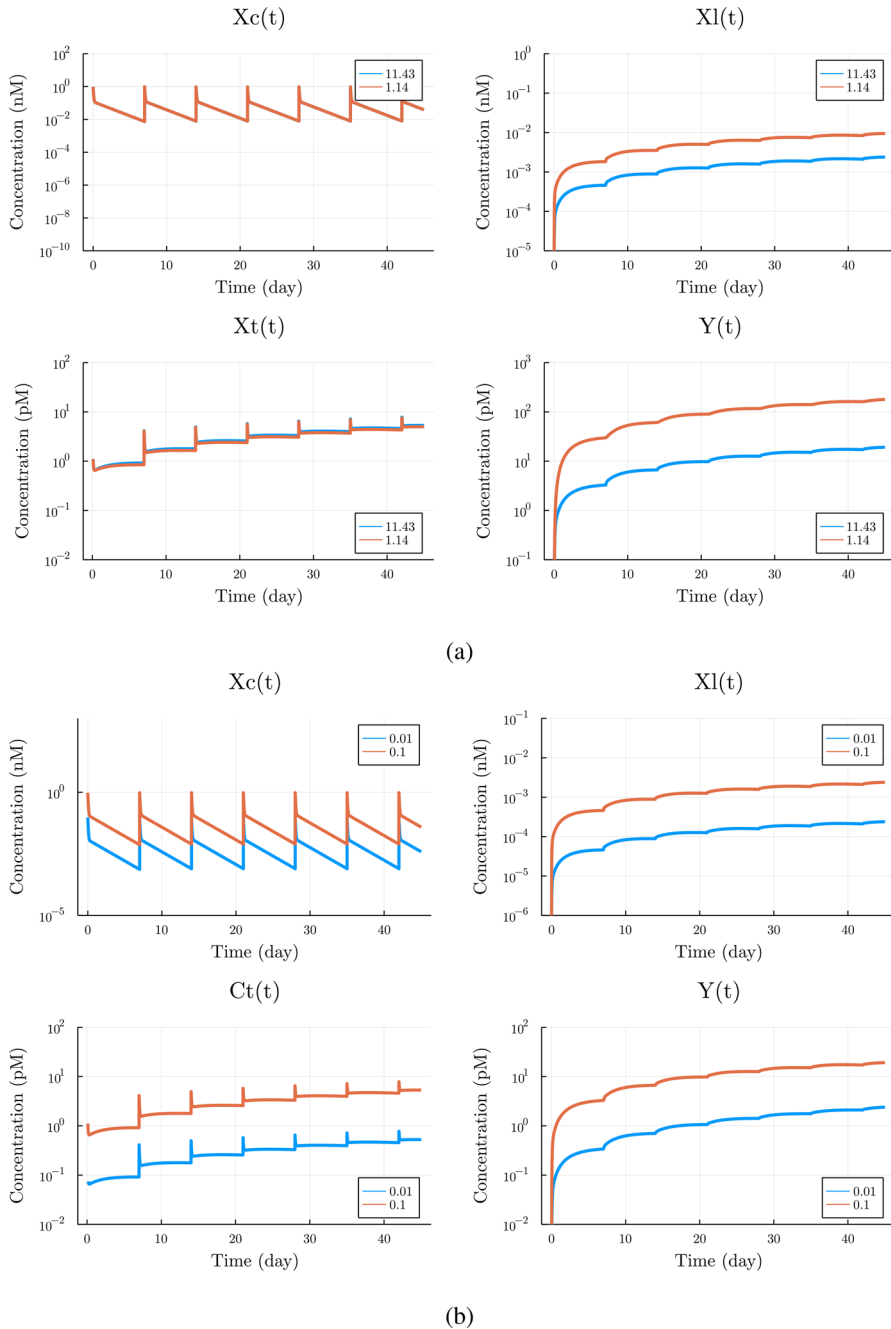
(a)

(b)

Fig. 7 Numerical simulations of the biodistribution model (3) for (a) different dissociation constant K_{D1} between TCE and immune cells and the same dose (labels represent K_{D1} in nM), and (b) different dose of TCE and the same dissociation constant (labels represent dosing levels in mg/kg).

these two molecules. The only difference between the two simulations is the value of k_{off_1}, which was adjusted to reflect a 10-fold difference in K_{D1}.

To better understand how a ten-fold change in the affinity can be compared with a ten-fold change in the drug dose, Figure 7bis presented. Notably, parameters α and β, defined as empirical parameters related to the lymph compartment, update the relationship with the dissociation constant K_{D1}.

3.4 Results on identifiability from steady state data

In this section, it is proved that the dissociation constants $K_{D1} = k_{\text{off}_1}/k_{\text{on}_1}$, and $K_{D2} = k_{\text{off}_2}/k_{\text{on}_2}$ are identifiable from just three generic steady state measurements that are different in the initial concentration of the TCE molecule with equal initial concentrations of the targets. By generic we mean that, for each exeperiment, there are only finitely many values of the initial concetrations to avoid; for the precise statement, see Theorem 1.

Several approaches to analyzing identifiability from steady states have been developed, see Gross (2016); Srinivasan et al. (2019), but they are not applicable directly to our specific setup (due to limited observations, multiple experiments with shared conserved quantities, etc).

Some of the proofs in this section rely on tedious symbolic computations which were performed on a computer. The corresponding code can be found in the *identifiability* folder of the repository [48] with the supplementary code for the paper.

In terms of state variables, consider a steady state X^*, T_1^*, T_2^*, D_1^*, D_2^*, Y^* of the system (1). Then the numbers X^*, T_1^*, T_2^*, D_1^*, D_2^*, Y^*, and k_{on_1}, k_{on_2}, k_{off_1}, k_{off_2} are related by a system of six polynomial equations obtained by setting the left-hand sides of (1) to zero, that is:

$$0 = -k_{\text{on}_1} T_1^* X^* - k_{\text{on}_2} T_2^* X^* + k_{\text{off}_1} D_1^* + k_{\text{off}_2} D_2^*, \tag{7a}$$

$$0 = -k_{\text{on}_1} T_1^* X^* + k_{\text{off}_1} D_1^* - k_{\text{on}_1} T_1^* D_2^* + k_{\text{off}_1} Y^*, \tag{7b}$$

$$0 = -k_{\text{on}_2} T_2^* X^* + k_{\text{off}_2} D_2^* - k_{\text{on}_2} T_2^* D_1^* + k_{\text{off}_2} Y^*, \tag{7c}$$

$$0 = k_{\text{on}_1} T_1^* X^* - k_{\text{off}_1} D_1^* - k_{\text{on}_2} T_2^* D_1^* + k_{\text{off}_2} Y^*, \tag{7d}$$

$$0 = k_{\text{on}_2} T_2^* X^* - k_{\text{off}_2} D_2^* - k_{\text{on}_1} T_1^* D_2^* + k_{\text{off}_1} Y^*, \tag{7e}$$

$$0 = k_{\text{on}_1} T_1^* D_2^* + k_{\text{on}_2} T_2^* D_1^* - (k_{\text{off}_1} + k_{\text{off}_2}) Y^*. \tag{7f}$$

We will start with establishing several properties of nonnegative steady states of the system (1).

Lemma 1 *Assume that the rate constants k_{on_1}, k_{on_2}, k_{off_1}, k_{off_2} are positive. Then, for every solution of the system (7) with nonnegative coordinates, the following hold:*

$$D_1^* D_2^* = X^* Y^*, \quad X^* T_1^* = k_{D_1} D_1^*, \quad and \quad X^* T_2^* = k_{D_2} D_2^*. \tag{8}$$

Proof The projection of the solution set on the coordinates $(D_1^*, D_2^*, X^*, Y^*, k_{\text{off}_1}, k_{\text{off}_2})$-coordinates (obtained by performing elimination with Gröbner bases (Cox et al.

(2005), Chapter 2, §1); the Maple code can be found in the supplementary materials
[48]) yields the following equation:

$$\left(D_1^* k_{\text{off}_1} + D_2^* k_{\text{off}_2} + X^* k_{\text{off}_1} + X^* k_{\text{off}_2}\right)\left(D_1^* D_2^* - X^* Y^*\right) = 0. \tag{9}$$

If the left bracket vanishes, then, by the positivity of the rate constants and nonneg-
ativity of the solution, we deduce $D_1^* = D_2^* = X^* = 0$, so $D_1^* D_2^* - X^* Y^* = 0$.
Otherwise, the right bracket must vanish, so the same equality holds. This gives us
the first equality in (8). Adding this equation to (7) and computing projections (again
with Gröbner bases) to $(D_1^*, D_2^*, X^*, k_{\text{off}_2}, k_{\text{on}_2}, T_2^*)$- and $(D_1^*, D_2^*, X^*, k_{\text{off}_1}, k_{\text{on}_1},$
$T_1^*)$-coordinates, respectively, we obtain that:

$$(X^* T_2^* k_{\text{on}_2} - D_2^* k_{\text{off}_2})(D_1^* - D_2^*) = 0,$$
$$(X^* T_1^* k_{\text{on}_1} - D_1^* k_{\text{off}_1})(D_1^* - D_2^*) = 0.$$

If $D_1^* \neq D_2^*$, the above equalities imply the last two equations from (8).

Now we assume that $D_1^* = D_2^*$, and add this equation to the system. By projecting
on $(D_2^*, X^*, k_{\text{off}_2}, k_{\text{on}_2}, T_2^*)$- and $(D_1^*, X^*, k_{\text{off}_1}, k_{\text{on}_1}, T_1^*)$-coordinates, respectively,
we obtain

$$(X^* + D_2^*)(X^* T_2^* k_{\text{on}_2} - D_2^* k_{\text{off}_2}) = 0,$$
$$(X^* + D_1^*)(X^* T_1^* k_{\text{on}_1} - D_1^* k_{\text{off}_1}) = 0.$$

In both equations above, vanishing of the left bracket would imply the vanishing of
the right, so the right one always vanishes. This yields the two remaining equations
of (8) and concludes the proof.   □

The three-body model (1) has three conservation laws:

$$c_1 = T_1(t) + D_1(t) + Y(t), \quad c_2$$
$$= T_2(t) + D_2(t) + Y(t), \quad \text{and } c_3 = X(t) + D_1(t) + D_2(t) + Y(t).$$

The set of nonegative states with the same values of c_1, c_2, c_3 is referred to as *stoi-
chiometric class*. Based on the initial conditions $D_1(0) = D_2(0) = Y(0) = 0$, we
have $c_1 = T_1(0), c_2 = T_2(0)$, and $c_3 = X(0)$. In the notation of Section 2.5, the
lemma below establishes that, for the set of trajectories $\mathcal{T}$ with these initial condi-
tions and satisfying $c_1, c_2, c_3 > 0$, the question of identifiability from steady states is
well-posed.

Lemma 2 (*cf. Ali Al-Radhawi et al.* (2020), *p. 11*) *Assume that the rate constants*
$k_{\text{on}_1}, k_{\text{on}_2}, k_{\text{off}_1}, k_{\text{off}_2}$ *are positive. Then, in each stoichiometric class (i.e., for every
positive values of c_1, c_2, c_3), there exists exactly one positive steady state which is glob-
ally asymptotically stable. Furthermore, its T_1^*- and T_2^*-coordinates are the unique
positive roots of*

$$(T_1^*)^2 + (c_3 + K_{D1} - c_1)T_1^* - c_1 K_{D1} = 0, \tag{10a}$$

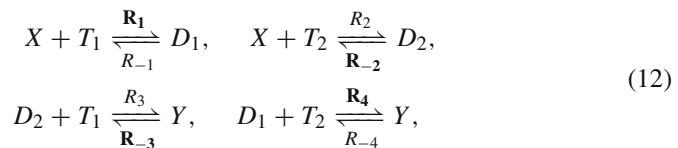**Fig. 8** Petri-net representation of the chosen irreversible subnetwork of (12).
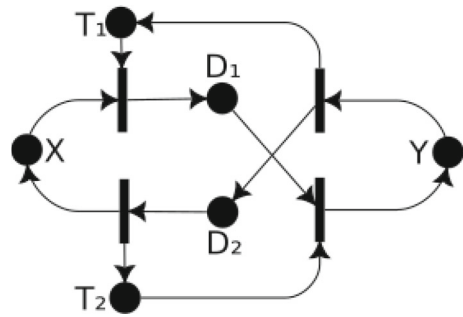
$$(T_2^*)^2 + (c_3 + K_{D2} - c_2)T_2^* - c_2 K_{D2} = 0, \tag{10b}$$

and the X*-coordinate satisfies

$$X^* = \frac{k_{\mathrm{off}_1}(T_2^* - c_2 + c_3) + k_{\mathrm{off}_2}(T_1^* - c_1 + c_3)}{(T_1^* k_{\mathrm{on}_1} + k_{\mathrm{off}_1} + T_2^* k_{\mathrm{on}_2} + k_{\mathrm{off}_2})}. \tag{11}$$

Proof The existence and uniqueness of globally asymptotically stable equilibrium was established in (Ali Al-Radhawi et al. (2020), p. 11). We recall the argument here. The system (4) can be represented by a chemical reaction network

$$
\begin{aligned}
X + T_1 &\underset{R_{-1}}{\overset{\mathbf{R_1}}{\rightleftharpoons}} D_1, \quad X + T_2 \underset{\mathbf{R_{-2}}}{\overset{R_2}{\rightleftharpoons}} D_2, \\
D_2 + T_1 &\underset{\mathbf{R_{-3}}}{\overset{R_3}{\rightleftharpoons}} Y, \quad D_1 + T_2 \underset{R_{-4}}{\overset{\mathbf{R_4}}{\rightleftharpoons}} Y,
\end{aligned}
\tag{12}
$$

with the rates $R_1 = k_{\mathrm{on}_1} T_1 X$, $R_{-1} = k_{\mathrm{off}_1} D_1$, $R_2 = k_{\mathrm{on}_2} T_2 X$, $R_{-2} = k_{\mathrm{off}_2} D_2$, $R_3 = k_{\mathrm{on}_1} D_2 T_1$, $R_{-3} = k_{\mathrm{off}_1} Y$, $R_4 = k_{\mathrm{on}_2} D_1 T_2$, and $R_{-4} = k_{\mathrm{off}_2} Y$.

The subnetwork of (12) consisting of the boldfaced reactions R_1, R_{-2}, R_{-3}, R_4 forms an M-network (see Ali Al-Radhawi et al. (2020), p. 29) and satisfies the requirements of (Ali Al-Radhawi et al. (2020), Theorem 40): each species participates in exactly one reaction and appears as a product of exactly one reaction, this is easy to see from the Petri net representation of the subnetwork on Figure 8. Therefore, by (Ali Al-Radhawi et al. (2020), Theorem 4) the function $\max \mathcal{R}(x) - \min \mathcal{R}(x)$, where

$$\mathcal{R} = \{R_1 - R_{-1}, \ R_{-2} - R_2, \ R_{-3} - R_3, \ R_4 - R_{-4}\},$$

is a convex robust Lyapunov function. The existence of such function implies the existence, uniqueness, and global stability of an equilibrium in every stoichiometric class.

We will now establish formulas (10) and (11). We augment the system (7) with the equations:

$$c_1 - T_1^* - D_1^* - Y^* = c_2 - T_2^* - D_2^* - Y^* = c_3 - X^* - Y^* - D_1^* - D_2^* = 0. \tag{13}$$

Given the obtained system of nine equations, we next compute the projections (again, using Gröbner bases; the Maple code can be found in the supplementary materials [48]) of the solution set onto the $(A, c_1, c_2, c_3, k_{\mathrm{on}_1}, k_{\mathrm{on}_2}, k_{\mathrm{off}_1}, k_{\mathrm{off}_2})$-coordinates, where A is taken to be T_1^* or T_2^*. We find that these projections satisfy precisely (10). Consider (10a) as a quadratic equation in T_1^*. The product of the roots is equal to $-c_2 K_{D2} < 0$, from which we conclude that there exists exactly one positive root, so it must be the T_1^*-coordinate of the unique steady state. The same applies to T_2^*.

Now we compute the projection onto the $(X^*, T_1^*, T_2^*, c_1, c_2, c_3, k_{\mathrm{on}_1}, k_{\mathrm{on}_2}, k_{\mathrm{off}_1}, k_{\mathrm{off}_2})$-coordinates and find a relation:

$$X^*(T_1^* k_{\mathrm{on}_1} + k_{\mathrm{off}_1} + T_2^* k_{\mathrm{on}_2} + k_{\mathrm{off}_2}) = k_{\mathrm{off}_1}(T_2^* - c_2 + c_3) + k_{\mathrm{off}_2}(T_1^* - c_1 + c_3). \tag{14}$$

The positivity of $T_1^* k_{\mathrm{on}_1} + k_{\mathrm{off}_1} + T_2^* k_{\mathrm{on}_2} + k_{\mathrm{off}_2}$ implies that we can express X^* uniquely and obtain (11). □

In other words, Lemma 2 shows that T_1^*, T_2^*, and X^* can be expressed as algebraic functions of $\mathbf{k} = (k_{\mathrm{on}_1}, k_{\mathrm{off}_1}, k_{\mathrm{on}_2}, k_{\mathrm{off}_2}) \in \mathbb{R}_{>0}^4$ and $c_1, c_2, c_3 \in \mathbb{R}_{>0}$. We will denote these functions by the same letter and write, for example $T_1^*(\mathbf{k}, c_1, c_2, c_3)$ for the positive root of (10a).

Next, we will consider several (two or three) experiments with the same $c_1 = T_1(0)$ and $c_2 = T_2(0)$ but varying $c_3 = X(0)$ (cf. Example 5). The next proposition establishes that the vector (K_{D_1}, K_{D_2}) is identifiable up to at most two possible values from the steady state data of two such experiments.

Proposition 1 *Consider two vectors $(T_1^{[i]}, T_2^{[i]}, X^{[i]}) \in \mathbb{R}_{>0}^3$ for $i = 1, 2$. Assume that*

$$(T_1^{[1]} - T_1^{[2]})(T_2^{[1]} - T_2^{[2]})(X^{[1]} T_1^{[1]} - X^{[2]} T_1^{[2]})(X^{[1]} T_2^{[1]} - X^{[2]} T_2^{[2]}) \neq 0. \tag{15}$$

Then, there exists a subset $\mathcal{K} \subset \mathbb{R}_{>0}$ of cardinality at most two such that, for every $\mathbf{k} \in \mathbb{R}_{>0}^4$, $c_1, c_2, c_3^{[1]}, c_3^{[2]} \in \mathbb{R}_{>0}$ satisfying

$$A^{[i]} = A^*(\mathbf{k}, c_1, c_2, c_3^{[i]})$$

for every $A \in \{T_1^*, T_2^*, X^*\}$ and $i = 1, 2$, we have $(K_{D_1}, K_{D_2}) = \left(\frac{k_{\mathrm{on}_1}}{k_{\mathrm{off}_1}}, \frac{k_{\mathrm{on}_2}}{k_{\mathrm{off}_2}}\right) \in \mathcal{K}$.

Furthermore, for every $\mathbf{k} \in \mathbb{R}_{>0}^4$ and $c_1, c_2, c_3^{[1]} \in \mathbb{R}_{>0}$, there are only finitely many values $c_3^{[2]} \in \mathbb{R}_{>0}$ such that (15) does not hold for $A^{[i]} = A^*(\mathbf{k}, c_1, c_2, c_3^{[i]})$, where $A \in \{T_1^*, T_2^*, X^*\}$ and $i = 1, 2$.

Proof Consider two vectors $(T_1^{[i]}, T_2^{[i]}, X^{[i]}) \in \mathbb{R}_{>0}^3$ for $i = 1, 2$ and $\mathbf{k} \in \mathbb{R}_{>0}^4$, $c_1, c_2, c_3^{[1]}, c_3^{[2]} \in \mathbb{R}_{>0}$ such that $A^{[i]} = A^*(\mathbf{k}, c_1, c_2, c_3^{[i]})$ for every $A \in \{T_1^*, T_2^*, X^*\}$

and $i = 1, 2$. We use (8) and equalities $D_1^* = c_1 - T_1^* - Y^*$ and $D_2^* = c_2 - T_2^* - Y^*$ to write the following polynomial system:

$$Y^{[i]} X^{[i]} = (c_1 - T_1^{[i]} - Y^{[i]})(c_2 - T_2^{[i]} - Y^{[i]}),$$
$$T_1^{[i]} X^{[i]} = K_{D1}(c_1 - T_1^{[i]} - Y^{[i]}),$$
$$T_2^{[i]} X^{[i]} = K_{D2}(c_2 - T_2^{[i]} - Y^{[i]}),$$
$$\text{for } i = 1, 2.$$

By computing the projection of the solution set of this system to the $(K_{D1}, K_{D2}, T_1^{[1]}, T_1^{[2]}, T_2^{[1]}, T_2^{[2]}, X^{[1]}, X^{[2]})$-coordinates (using Gröbner bases), we find expressions of the form:

$$A_1 K_{D1}^2 + A_2 K_{D1} + A_3 = 0, \tag{16a}$$
$$B_1 K_{D2} + B_2 K_{D1} + B_3 = 0, \tag{16b}$$

where $A_1, A_2, A_3, B_1, B_2, B_3$ are polynomials from $\mathbb{Q}[T_1^{[i]}, T_2^{[i]}, X^{[i]} \mid i = 1, 2]$. Furthermore, A_1 and B_1 factor as follows:

$$A_1 = X^{[1]} X^{[2]} (T_1^{[1]} - T_1^{[2]})(T_2^{[1]} X^{[1]} - T_2^{[2]} X^{[2]}), \tag{17a}$$
$$B_1 = X^{[1]} X^{[2]} (T_2^{[1]} - T_2^{[2]})(T_1^{[1]} X^{[1]} - T_1^{[2]} X^{[2]}). \tag{17b}$$

Therefore, if (15) holds, A_1 and B_1 do not vanish. Then K_{D_1} must be one of the roots of (16a) and then K_{D_2} is uniquely determined from (16b). Since the coefficients of the equations (16a) and (16b) depend only on $T_1^{[i]}, T_2^{[i]}, X^{[i]}$ for $i = 1, 2$, these two solutions form the set $\mathcal{K}$ from the statement of the proposition.

In order to prove the second statement of the proposition, we fix $\mathbf{k} \in \mathbb{R}_{>0}^4$ and $c_1, c_2, c_3^{[1]} \in \mathbb{R}_{>0}$ and consider $T_1^{[2]}, T_2^{[2]}$, and $X^{[2]}$ as functions in $c_3 = c_3^{[2]}$. By Lemma 2, these functions are algebraic. We notice that (15) is equivalent to inequalities:

$$T_1^{[1]} \neq T_1^{[2]}, \quad T_2^{[1]} \neq T_2^{[2]}, \quad X^{[1]} T_1^{[1]} \neq X^{[2]} T_1^{[2]}, \quad X^{[1]} T_2^{[1]} \neq X^{[2]} T_2^{[2]}.$$

Since a nonconstant univariate algebraic function takes each value only finitely many times, it is sufficient to prove that the functions

$$T_1^{[2]}(c_3), \quad T_2^{[2]}(c_3), \quad X^{[2]}(c_3) T_1^{[2]}(c_3), \quad X^{[2]}(c_3) T_2^{[2]}(c_3) \tag{18}$$

are nonconstant. To this end, we use (10a) and (10b) to write the Taylor series for $T_1^{[2]}$ and $T_2^{[2]}$ at $c_3 = 0$:

$$T_1^{[2]}(c_3) = c_1 - \frac{c_1}{c_1 K_{D_1} + 1} c_3 + \mathcal{O}(c_3^2) \quad \text{and} \quad T_2^{[2]}(c_3)$$

$$= c_2 - \frac{c_2}{c_2 K_{D_2} + 1} c_3 + \mathcal{O}(c_3^2).$$

By plugging these to (11), we obtain an expansion for $X^{[2]}$:

$$X^{[2]}(c_3) = \frac{\left(\frac{k_{\text{off}_2}}{c_1 K_{D_1}+1} + \frac{k_{\text{off}_1}}{c_2 K_{D_2}+1}\right) c_3 + \mathcal{O}(c_3)^2}{c_1 k_{\text{on}_1} + c_2 k_{\text{on}_2} + k_{\text{off}_1} + k_{\text{off}_2} + \mathcal{O}(c_3)}$$

$$= \frac{\frac{k_{\text{off}_2}}{c_1 K_{D_1}+1} + \frac{k_{\text{off}_1}}{c_2 K_{D_2}+1}}{c_1 k_{\text{on}_1} + c_2 k_{\text{on}_2} + k_{\text{off}_1} + k_{\text{off}_2}} c_3 + \mathcal{O}(c_3^2).$$

From these expansions, we see that indeed none of the functions (18) is constant. This finished the proof of the second claim of the proposition. $\qquad\square$

The following theorem establishes that, using the terminology of Section 2.5, the vector (K_{D_1}, K_{D_2}) is globally identifiable from the steady state data for three generic experiments with the same values of c_1, c_2 but varying value of c_3.

Theorem 1 (Unique identifiability from three experiments) *Consider three vectors* $(T_1^{[i]}, T_2^{[i]}, X^{[i]}) \in \mathbb{R}^3_{>0}$ *for* $i = 1, 2, 3$. *Assume that*

$$R_2 \neq R_3 \quad or \quad R_2 < 0 \quad or \quad R_3 < 0, \tag{19}$$

where

$$R_i := \frac{(T_1^{[1]} - T_1^{[i]})(X^{[1]}T_2^{[1]} - X^{[i]}T_2^{[i]})}{(X^{[1]}T_1^{[1]} - X^{[i]}T_1^{[i]})(X^{[1]}T_1^{[1]}T_2^{[1]} - X^{[i]}T_1^{[i]}T_2^{[i]})} \quad for \ i = 2, 3.$$

Then there exists a vector $\mathbf{k}_D \in \mathbb{R}^2_{>0}$ *such that for every* $\mathbf{k} \in \mathbb{R}^4_{>0}, c_1, c_2, c_3^{[1]}, c_3^{[2]}, c_3^{[3]} \in \mathbb{R}_{>0}$ *satisfying*

$$A^{[i]} = A^*(\mathbf{k}, c_1, c_2, c_3^{[i]})$$

for every $A \in \{T_1^*, T_2^*, X^*\}$ *and* $i = 1, 2, 3$, *we have* $\left(\frac{k_{\text{on}_1}}{k_{\text{off}_1}}, \frac{k_{\text{on}_2}}{k_{\text{off}_2}}\right) = \mathbf{k}_D$.

Furthermore, for every $\mathbf{k} \in \mathbb{R}^4_{>0}$ *and* $c_1, c_2, c_3^{[1]}, c_3^{[2]} \in \mathbb{R}_{>0}$, *there are only finitely many values* $c_3^{[3]} \in \mathbb{R}_{>0}$ *such that* (19) *does not hold for* $A^{[i]} = A^*(\mathbf{k}, c_1, c_2, c_3^{[i]})$, *where* $A \in \{T_1^*, T_2^*, X^*\}$ *and* $i = 1, 2, 3$.

Proof The proof strategy will be similar to the one for Proposition 1. Consider two vectors $(T_1^{[i]}, T_2^{[i]}, X^{[i]}) \in \mathbb{R}^3_{>0}$ for $i = 1, 2, 3$ and $\mathbf{k} \in \mathbb{R}^4_{>0}, c_1, c_2, c_3^{[1]}, c_3^{[2]}, c_3^{[3]} \in \mathbb{R}_{>0}$ such that $A^{[i]} = A^*(\mathbf{k}, c_1, c_2, c_3^{[i]})$ for every $A \in \{T_1^*, T_2^*, X^*\}$ and $i = 1, 2, 3$.

Consider the relations (16a) and (16b) obtained in the proof of Proposition 1. Recall that (17a):

$$A_1 = X^{[1]}X^{[2]}(T_1^{[1]} - T_1^{[2]})(T_2^{[1]}X^{[1]} - T_2^{[2]}X^{[2]}).$$

Furthermore, we have

$$A_3 = X^{[1]}X^{[2]}(X^{[1]}T_1^{[1]} - X^{[i]}T_1^{[i]})(X^{[1]}T_1^{[1]}T_2^{[1]} - X^{[i]}T_1^{[i]}T_2^{[i]}).$$

Therefore, $R_2 = \frac{A_1}{A_3}$. If $R_2 < 0$, then (16a) has exactly one positive root. In this case, k_{D_1} would be uniquely determined, and then k_{D_2} would be uniquely determined from (16b). The same argument applies to $R_3 < 0$ due to the symmetry between the second and the third experiment.

In order to take into account the third experiment, we apply the derivation of (16a) and (16b) from the proof of Proposition 1 to the first and third vectors instead of the first and the second. This way, $T_1^{[2]}, T_2^{[2]}, X^{[2]}$ in (16a) will be replaced with $T_1^{[3]}, T_2^{[3]}, X^{[3]}$, and the resulting relation will also be true. This will yield one more quadratic equation for K_{D1}, which we will denote by $\widetilde{A}_1 K_{D1}^2 + \widetilde{A}_2 K_{D1} + \widetilde{A}_3 = 0$. Since $\widetilde{A}_1$ and $\widetilde{A}_3$ are obtained from A_1 and A_3 by replacing $T_1^{[2]}, T_2^{[2]}, X^{[2]}$ with $T_1^{[3]}, T_2^{[3]}, X^{[3]}$, we have $R_3 = \frac{\widetilde{A}_1}{\widetilde{A}_3}$. If $R_2 \neq R_3$, then the quadratic equations (16a) and $\widetilde{A}_1 K_{D1}^2 + \widetilde{A}_2 K_{D1} + \widetilde{A}_3 = 0$ are not proportional, so they have at most one common root thus leaving at most one possible value for k_{D_1}.

In order to prove the second part of the theorem, we fix $\mathbf{k} \in \mathbb{R}_{>0}^4$ and $c_1, c_2, c_3^{[1]} \in \mathbb{R}_{>0}$, and consider the function

$$f(c_3) := \frac{(T_1^{[1]} - T_1^*(c_3))(X^{[1]}T_2^{[1]} - X^*(c_3)T_2^*(c_3))}{(X^{[1]}T_1^{[1]} - X^*(c_3)T_1^*(c_3))(X^{[1]}T_1^{[1]}T_2^{[1]} - X^*(c_3)T_1^*(c_3)T_2^*(c_3))}.$$

Then we have $R_2 = f(c_3^{[2]})$ and $R_3 = f(c_3^{[3]})$. By Lemma 2, $f(c_3)$ is an algebraic function. Therefore, if it is a nonconstant algebraic function, it takes each value only finitely many times, so the equality $R_2 = R_3$ will be true only for finitely many values of $c_3^{[3]}$ as desired. Now assume that $f(c_3)$ is a constant function. Then $R_2 = f(c_3^{[2]}) = f(0)$. Using $X^*(0) = 0$ and $T_1^*(0) = c_1$, we find that

$$f(0) = \frac{(T_1^{[1]} - c_1)}{(X^{[1]}T_1^{[1]})^2}.$$

Since $c_1 = T_1^{[1]} + D_1^{[1]} + Y^{[1]}$, we have $T_1^{[1]} < c_1$, so $f(0) < 0$. This implies $R_2 < 0$, so (19) is fulfilled independently of the value of $c_3^{[3]}$.   □

We will illustrate the above argument with a numerical example. We will first take the initial concentrations and parameter values the same as in the example in the introduction:

$$X(0) = 1.0, \ T_1(0) = 1.08 \cdot 10^{-1}, \ T_2(0) = 166, \ D_1(0) = D_2(0) = Y(0) = 0,$$
$$k_{n_1} = 1.72, \ k_{f_1} = 19.66, \ k_{n_2} = 1.57, \ k_{f_2} = 0.74.$$

Through numerical simulations, we compute the values of X, T_1, T_2 at the steady state: $X^{[1]} = 2.8 \cdot 10^{-3}, T_1^{[1]} = 9.9 \cdot 10^{-2}, T_2^{[1]} = 165$. Next, we simulate one more

experiment with all the initial conditions staying the same except for $X(0) = 1.1$. The new steady state is $X^{[2]} = 3.1 \cdot 10^{-3}$, $T_1^{[2]} = 9.8 \cdot 10^{-2}$, $T_2^{[2]} = 164.9$. Plugging these values into equations (16), we find two solutions for (K_{D1}, K_{D2}) one of which is equal to the true values, and the other one is negative and can therefore be discarded. So, in this case, two experiments are sufficient to find the unique parameter values. Even if the second solution of (16) was positive, it could be discarded by performing one more experiment with different $X(0)$, and choosing the solution of (16) appearing among the solutions of (16) for the first pair of experiments.

The details of all the symbolic and numeric calculations from this section can be found in the *identifiability* folder of the repository [48] with the supplementary code for the paper.

4 Discussion

Although each of the TCEs presented in this study was designed for a different cancer cell target, the initial concentration of the targets on cancer cells is assumed to be equally expressed on the cancer cell surface to visualize the quantitative differences between the bell-shapes in Figure 5.

From the three-body model perspective, a promising TCE antibody is the one that creates the largest trimer concentration with the minimal initial concentration of the antibody at the site of action. Additionally, to overcome natural intra-tumoral and inter-patient variability, it is favorable to have a TCE antibody with minimal variation for different ratios of the initial concentrations of the targets. So, a TCE antibody molecule is effective at the site of action if it results in: 1) a relatively higher peak of the trimer concentration at the site of action, 2) a relatively lower exposure in the circulating compartment to avoid toxicity issues, 3) lower affinity toward CD3 to prevent drug sing in the non-tumor compartments, and 4) robust characteristics of the bell-shape for different range of target concentrations, to have the highest predictability for different initial conditions across patients and tumors.

Among the molecules presented in Figure 6, it can be observed that the 7370, and PF-06671008 molecules are projected to have the largest concentrations of trimers in TME with minimal initial target concentrations. On the other hand, Solitomab creates a stable width of the peak for a wide range of ratios between the initial concentrations of the targets. It is apparent that stability across different initial concentrations of the targets increases the consistency of the data in clinical research.

In addition to the TCE molecules presented in Table 1, other molecules are discussed in detail in the literature. PF-06863135 Panowski (2019) (150 kDa), and AMG420 Hipp (2017) (54 kDa) are both designed to target B-Cell Maturation Antigen (BCMA) for patients diagnosed with multiple myeloma. Both of the molecules have similar dissociation constants to CD3, but different dissociation constants to BCMA, 0.1 and 0.04 nM respectively. The role of binding kinetics to BCMA is discussed as an important factor in the distribution of the molecule toward different tissues in Hipp (2017). Also, the authors of Moek (2019) discussed the design and bio-distribution of AMG211 (55 kDa), a CD3/CEA TCE molecule for patients with advanced gastrointestinal adeno-carcinomas. AMG211 has a significantly high dissociation constant to CD3 310 nM

in comparison with its dissociation constant toward CEA 5.5 nM. The biodistributions of these molecules are explained by a computational model in Yoneyama (2021).

A molecule with a bell-shaped efficacy curve will have an important property: its efficacy will be maximized at the concentrations that correspond to the peak of trimer formation (Figure 1(b), yellow thick line), and will be low at the concentrations that are significantly less or significantly higher than that. This provides an opportunity to assess the predictions in the following way: with the understanding of PK properties of the desired compound, one can calculate doses (using standard PK-PD modeling methodology) that will achieve steady state concentrations in the tumor microenvironment below, at, or beyond the drug concentrations predicted to maximize efficacy. One can then design a pre-clinical experiment, where animals receive drug doses that will achieve these concentrations, and assess, whether efficacy is optimized at the intermediate "optimal" concentration. It should be noted that because it takes time for a drug to accumulate in the TME, it may take time to see the difference between the dosing regimens, with the higher-dose regimen achieving higher efficacy short term (it will reach the "optimal" drug concentration sooner) but will then lose efficacy in the longer term, since drug will continue accumulating, and therefore will soon move into the suboptimal range on the right of the efficacy curve.

Interestingly, if one were to evaluate the dosing regimens of some of the approved TCEs, one would observe that epcrotitamab (anti-CD3/anti-CD20) protocol dictates increasing spaces between doses, with the drug given weekly during the first three treatment cycles, then given at 48 mg every 2 weeks between 4th-9th treatment cycles, and finally every 4 weeks after the 10th treatment cycle. Glofitamab, another highly efficacious anti-CD3/anti-CD20 antibody, is given at 30 mg every 2 weeks for the first treatment cycle, and then every 4 weeks for subsequent cycles. Mosunetuzumab starts with weekly dosing, with 60 mg given every 3 weeks for the second treatment cycle, and then lowering the dose to 30mg for subsequent treatment cycles. All of these (increasing spacing between doses or lowering dosing for later treatment cycles) could be potential mitigation strategies to ensure that the drug concentration remains in the "optimal" zone.

The simplified three-body model provides valuable initial insights, but it may not fully capture the complexity of TCE interactions *in vivo*. Tailored version of this model for each target to incorporate factors such as T cell dynamics, tumor heterogeneity, and drug disposition would improve the model's predictive accuracy for clinical applications for future programs.

A common safety concern for TCEs is cytokine release syndrome (CRS), which arises from excessive immune activation and leads to a surge in inflammatory cytokines with potentially severe systemic effects. While the present study focuses on characterizing dose-response relationships with respect to efficacy-using maximum trimer concentration as a key feature-understanding the full therapeutic window will ultimately require integrating both efficacy and safety considerations.

In particular, the bell-shaped nature of the dose-response curve suggests that exceeding a certain concentration could result not only in reduced efficacy but also in heightened toxicity risk. Thus, future modeling efforts should aim to incorporate safety endpoints, such as cytokine profiles or clinical markers of CRS, to better inform dose selection. A recent review of clinical dose optimization strategies for T-cell-enhanced

therapies highlights various dosing approaches and emphasizes the importance of customized dosing regimens via mathematical modeling in the future Ball (2023).

Additionally, while our study emphasizes the peak of the bell-shaped curve as a marker of maximum efficacy, we recognize that this alone is not sufficient to fully characterize the dose-response relationship. We complement our peak-focused sensitivity analysis with numerical comparisons of the curve width (e.g., Figure 6), which offer insight into the robustness and breadth of the therapeutic window. A more comprehensive modeling framework-including toxicity metrics and safety thresholds-will be necessary to support clinical dose optimization, and this remains an important direction for future work.

The proposed analysis can be used to further assess the optimal properties for the design of CD3-based bispecific T cell engagers for a variety of scenarios and targets, to hopefully expand the applicability of this modality to a larger number of indications.

Author Contributions MS, IK, GP, and EDS wrote the manuscript; MS, IK, and EDS designed the research; MS and GP performed the research; MS, IK, and EDS analyzed the data.

References

Mellman I, Coukos G, Dranoff G (2011) Cancer immunotherapy comes of age. Nature 480(7378):480–489

Goleva E et al (2021) Our current understanding of checkpoint inhibitor therapy in cancer immunotherapy. Annals of Allergy, Asthma & Immunology 126(6):630–638

Feins S et al (2019) An introduction to chimeric antigen receptor (CAR) T-cell immunotherapy for human cancer. American Journal of Hematology 94(S1):S3–S9

Bonaventura P et al (2019) Cold tumors: a therapeutic challenge for immunotherapy. Frontiers in Immunology 10:168

Liu Y-T, Sun Z-J (2021) Turning cold tumors into hot tumors by improving T-cell infiltration. Theranostics 11(11):5365

Stieglmaier J, Benjamin J, Nagorsen D (2015) Utilizing the BiTE (bispecific T-cell engager) platform for immunotherapy of cancer. Expert Opinion on Biological Therapy 15(8):1093–1099

Yuraszeck T, Kasichayanula S, Benjamin J (2017) Translation and clinical development of bispecific T-cell engaging antibodies for cancer treatment. Clinical Pharmacology & Therapeutics 101(5):634–645

Betts A, van der Graaf PH (2020) Mechanistic quantitative pharmacology strategies for the early clinical development of bispecific antibodies in oncology. Clinical Pharmacology & Therapeutics 108(3):528–541

Tian Z et al (2021) Bispecific T cell engagers: an emerging therapy for management of hematologic malignancies. Journal of Hematology & Oncology 14(1):1–18

Laszlo GS et al (2014) Cellular determinants for preclinical activity of a novel CD33/CD3 bispecific T-cell engager (BiTE) antibody, AMG 330, against human AML. Blood, The Journal of the American Society of Hematology 123(4):554–561

Hipp S et al (2017) A novel BCMA/CD3 bispecific T-cell engager for the treatment of multiple myeloma induces selective lysis in vitro and in vivo. Leukemia 31(8):1743–1751

Topp MS et al (2014) Phase II trial of the anti-CD19 bispecific T cell-engager blinatumomab shows hematologic and molecular remissions in patients with relapsed or refractory B-precursor acute lymphoblastic leukemia. Journal of Clinical Oncology 32(36):4134–4140

Kebenko M et al (2018) A multicenter phase 1 study of solitomab (MT110, AMG 110), a bispecific EpCAM/CD3 T-cell engager (BiTE®) antibody construct, in patients with refractory solid tumors. Oncoimmunology 7(8):e1450710

Einsele H et al (2020) The BiTE (bispecific T-cell engager) platform: development and future potential of a targeted immuno-oncology therapy across tumor types. Cancer 126(14):3192–3201

Morcos PN et al (2021) Quantitative clinical pharmacology of T-Cell engaging bispecifics: current perspectives and opportunities. Clinical and Translational Science 14(1):75–85

Drake CG et al (2020) "A phase I/II study of REGN5678 (Anti-PSMAxCD28, a costimulatory bispecific antibody) with cemiplimab (anti-PD-1) in patients with metastatic castration-resistant prostate cancer". In: *American Society of Clinical Oncology*

Zhang J et al (2021) *A phase I/II study of REGN5678 (Anti-PSMAxCD28, a costimulatory bispecific antibody) with cemiplimab (anti–PD-1) in patients with metastatic castration-resistant prostate cancer.*

Lee JJ et al (2010) Emax model and interaction index for assessing drug interaction in combination studies. Frontiers in Bioscience (Elite edition) 2:582

Betts A et al (2019) A translational quantitative systems pharmacology model for CD3 bispecific molecules: application to quantify T cell-mediated tumor cell killing by P-cadherin LP DART&reg. I The AAPS Journal 21(4):1–16

Dreier T et al (2002) Extremely potent, rapid and costimulation-independent cytotoxic T-cell response against lymphoma cells catalyzed by a single-chain bispecific antibody. International Journal of Cancer 100(6):690–697

Brischwein K. et al. "MT110: a novel bispecific single-chain antibody construct with high efficacy in eradicating established tumors". In: *Molecular Immunology* 43.8 (2006), pp.1129–1143

Friedrich M et al (2012) Regression of human prostate cancer xenografts in mice by AMG 212/BAY2010112, a novel PSMA/CD3-Bispecific BiTE antibody cross-reactive with non-human primate antigens. Molecular Cancer Therapeutics 11(12):2664–2673

Root AR et al (2016) Development of PF-06671008, a highly potent anti-P-cadherin/anti-CD3 bispecific DART molecule with extended half-life for the treatment of cancer. Antibodies 5(1):6

Mandikian D et al (2018) Relative target affinities of T-cell-dependent bispecific antibodies determine biodistribution in a solid tumor mouse model. Molecular Cancer Therapeutics 17(4):776–785

Yeung YA et al (2020) An optimized full-length FLT3/CD3 bispecific antibody demonstrates potent anti-leukemia activity and reversible hematological toxicity. Molecular Therapy 28(3):889–900

Mathur D et al (2020) A novel GUCY2C-CD3 T-cell engaging bispecific construct (PF-07062119) for the treatment of gastrointestinal cancers. Clinical Cancer Research 26(9):2188–2202

Giffin MJ et al (2021) AMG 757, a half-life extended, DLL3-targeted bispecific T-cell engager, shows high potency and sensitivity in preclinical models of small-cell lung cancer. Clinical Cancer Research 27(5):1526–1537

Deegen P et al (2021) The PSMA-targeting half-life extended BiTE therapy AMG 160 has potent antitumor activity in preclinical models of metastatic castration-resistant prostate cancer. Clinical Cancer Research 27(10):2928–2937

Yadav R et al (2022) Nonclinical Pharmacokinetics and Pharmacodynamics Characterization of Anti-CD79b/CD3 T Cell-Dependent Bispecific Antibody Using a Surrogate Molecule: A Potential Therapeutic Agent for B Cell Malignancies. Pharmaceutics 14(5):970

Jordan SC et al (2020) The role of novel therapeutic approaches for prevention of allosensitization and antibody-mediated rejection. American Journal of Transplantation 20:42–56

Douglass EF Jr et al (2013) A comprehensive mathematical model for three-body binding equilibria. Journal of the American Chemical Society 135(16):6092–6099

De Boer RJ, Perelson AS (2013) Quantifying T lymphocyte turnover. Journal of Theoretical Biology 327:45–87

Smith E et al. *Bispecific anti-BCMA x anti-CD3 antibodies and uses thereof*. US Patent App. 16/516,028. Jan. (2020)

Rhoden JJ, Dyas GL, Wroblewski VJ (2016) A modeling and experimental investigation of the effects of antigen density, binding affinity, and antigen expression ratio on bispecific antibody binding to cell surface targets. Journal of Biological Chemistry 291(21):11337–11347

Sengers B.G et al (2016) "Modeling bispecific monoclonal antibody interaction with two cell membrane targets indicates the importance of surface diffusion". *MAbs*. Vol.8. 5. Taylor & Francis. pp.905–915

Harms BD et al (2014) Understanding the role of cross-arm binding efficiency in the activity of monoclonal and multispecific therapeutic antibodies. Methods 65(1):95–104

Kaufman EN, Jain RK (1992) Effect of bivalent interaction upon apparent antibody affinity: experimental confirmation of theory using fluorescence photobleaching and implications for antibody binding assays. Cancer Research 52(15):4157–4167

Thurber GM, Wittrup KD (2012) A mechanistic compartmental model for total antibody uptake in tumors. Journal of Theoretical Biology 314:57–68

Miao H et al (2011) On identifiability of nonlinear ODE models and applications in viral dynamics. SIAM Review 53(1):3–39. https://doi.org/10.1137/090757009

Hong H et al (2020) Global identifiability of differential models. Communications on Pure and Applied Mathematics 73(9):1831–1879. https://doi.org/10.1002/cpa.21921

Barreiro XR, Villaverde AF (2023) "Benchmarking tools for a priori identifiability analysis". In: *Bioinformatics* 39.2. https://doi.org/10.1093/bioinformatics/btad065

Ilmer I, Ovchinnikov A, Pogudin G (2021)"Web-based structural identifiability analyzer". *Computational Methods in Systems Biology*. , pp.254–265. https://doi.org/10.1007/978-3-030-85633-5_17

Hong H et al (2019) SIAN: software for structural identifiability analysis of ODE models. Bioinformatics 35(16):2873–2874

Ovchinnikov A et al (2021) Computing all identifiable functions of parameters for ODE models. Systems & Control Letters 157:105030. https://doi.org/10.1016/j.sysconle.2021.105030

Sontag E (2001) Structure and stability of certain chemical networks and applications to the kinetic proofreading model of T-cell receptor signal transduction. IEEE Transactions on Automatic Control 46(7):1028–1047. https://doi.org/10.1109/9.935056

Bezanson J et al (2017) Julia: A fresh approach to numerical computing. SIAM Review 59(1):65–98

Rackauckas C, Nie Q (2017) "DifferentialEquations.jl – a performant and feature-rich ecosystem for solving differential equations in Julia". In: *The Journal of Open Research Software* 5.1. https://doi.org/10.5334/jors.151

Supplementary code. 2023. https://github.com/mahdiarsadeghi/bites

Gross E et al (2016) Algebraic systems biology: a case study for the Wnt pathway. Bulletin of Mathematical Biology 78:21–51. https://doi.org/10.1007/s11538-015-0125-1

Srinivasan S, Cluett WR, Mahadevan R (2019) A scalable method for parameter identification in kinetic models of metabolism using steady-state data. Bioinformatics 35(24):5216–5225. https://doi.org/10.1093/bioinformatics/btz445

Cox DA, Little J, O'Shea D (2005) *Using Algebraic Geometry*. Springer New York, NY. https://doi.org/10.1007/b138611

Ali Al-Radhawi M, Angeli D, Sontag ED (2020) "A computational framework for a Lyapunov-enabled analysis of biochemical reaction networks". *PLoS Computational Biology* 16.2 , e1007681

Panowski SH et al (2019) Preclinical efficacy and safety comparison of CD3 bispecific and ADC modalities targeting BCMA for the treatment of multiple myeloma. Molecular Cancer Therapeutics 18(11):2008–2020

Moek KL et al (2019) 89Zr-labeled bispecific T-cell engager AMG 211 PET shows AMG 211 accumulation in CD3-rich tissues and clear, heterogeneous tumor uptake89Zr-bispecific T-cell engager PET in patients with cancer. Clinical Cancer Research 25(12):3517–3527

Yoneyama T et al (2021) "Leveraging a physiologically based quantitative translational modeling platform for designing bispecific T cell engagers for treatment of multiple myeloma". In: *bioRxiv*

Ball K et al (2023) "Strategies for clinical dose optimization of T cell-engaging therapies in oncology". In: *MAbs*. Vol.15. 1. Taylor & Francis. p.2181016